The Astrophysical Journal, 864:165 (17pp), 2018 September 10 https://doi.org/10.3847/1538-4357/aad9f7

A Model for Coronal Hole Bright Points and Jets Due to Moving Magnetic Elements

P. F. Wyper[1], C. R. DeVore[2], J. T. Karpen[2], S. K. Antiochos[2], and A. R. Yeates[1]
[1] Department of Mathematical Sciences, Durham University, Durham, DH1 3LE, UK; peter.f.wyper@durham.ac.uk, anthony.yeates@durham.ac.uk
[2] Heliophysics Science Division, NASA Goddard Space Flight Center, 8800 Greenbelt Road, Greenbelt, MD 20771, USA; c.richard.devore@nasa.gov, judith.t.karpen@nasa.gov, spiro.antiochos@nasa.gov
Received 2018 May 21; revised 2018 August 8; accepted 2018 August 9; published 2018 September 13

Abstract

Coronal jets and bright points occur prolifically in predominantly unipolar magnetic regions, such as coronal holes (CHs), where they appear above minority-polarity intrusions. Intermittent low-level reconnection and explosive, high-energy-release reconnection above these intrusions are thought to generate bright points and jets, respectively. The magnetic field above the intrusions possesses a spine-fan topology with a coronal null point. The movement of magnetic flux by surface convection adds free energy to this field, forming current sheets and inducing reconnection. We conducted three-dimensional magnetohydrodynamic simulations of moving magnetic elements as a model for coronal jets and bright points. A single minority-polarity concentration was subjected to three different experiments: a large-scale surface flow that sheared part of the separatrix surface only, a large-scale surface flow that also sheared part of the polarity inversion line surrounding the minority flux, and the latter flow setup plus a "flyby" of a majority-polarity concentration past the moving minority-polarity element. We found that different bright-point morphologies, from simple loops to sigmoids, were created. When only the field near the separatrix was sheared, steady interchange reconnection modulated by quasi-periodic, low-intensity bursts of reconnection occurred, suggestive of a bright point with periodically varying intensity. When the field near the polarity inversion line was strongly sheared, on the other hand, filament channels repeatedly formed and erupted via the breakout mechanism, explosively increasing the interchange reconnection and generating nonhelical jets. The flyby produced even more energetic and explosive jets. Our results explain several key aspects of CH bright points and jets, and the relationships between them.

Key words: magnetic reconnection – Sun: activity – Sun: corona – Sun: magnetic fields

Supporting material: animations

1. Introduction

Small brightenings and impulsive flows are found throughout the "quiet" solar corona, in association with photospheric magnetic-field concentrations and parasitic-polarity intrusions. These features are most visible as bright points and jets in coronal holes (CHs), where the background magnetic field is largely unipolar and open, and the ambient plasma is dark in EUV and X-ray wavelengths. Coronal bright points are seen as enhanced EUV and X-ray emission from small regions with diameters on the order of 10–50 arcsec, and lifetimes of 3–60 hr in EUV (Zhang et al. 2001; Mou et al. 2016) and up to 8 hr in X-rays (Golub et al. 1974). A puzzling feature of most bright points is that their intensity varies periodically, with periods ranging from a few minutes up to a couple of hours (Kariyappa & Varghese 2008; Tian et al. 2008). Their internal morphology appears to be similar in CHs and quiet Sun (Habbal et al. 1990; Galsgaard et al. 2017): bright points can contain a sigmoid (e.g., Brown et al. 2001), a few parallel loops (Zhang et al. 2012), or an anemone (e.g., Shibata et al. 1994). In many cases, bright points are associated with moving magnetic elements (MMEs), sometimes with opposite-polarity concentrations separating from each other due to flux emergence, at other times converging toward each other to coalesce and cancel (Webb et al. 1993; Mou et al. 2016). These associations with interactions between opposite-polarity magnetic fields have led to broad acceptance that bright points ultimately derive their energy from magnetic reconnection and the ensuing acceleration and heating of the entrained plasma.

Long-lived bright points are frequently observed to produce coronal jets: impulsive, collimated flows of dense, hot plasma, which are launched low in the atmosphere and are guided along the ambient coronal magnetic field (Shimojo et al. 1996; Nisticò et al. 2009; Raouafi et al. 2016). Jets have much shorter lifetimes (a few minutes) than bright points (Savcheva et al. 2007), so an individual bright point can produce multiple jets over its lifetime. Some jets extend so far into the corona that they can be observed in scattered white light in the inner heliosphere (e.g., Wang et al. 1998), thus contributing mass, momentum, and distinct structures to the solar wind. High-resolution observations have revealed that many, if not most, jets contain miniature filaments (cool plasma) and/or sigmoids (hot plasma) that erupt to generate the jet (e.g., Innes et al. 2009; Raouafi et al. 2010; Shen et al. 2012; Hong et al. 2014, 2016; Sterling et al. 2015, 2016; Kumar et al. 2018). Typically, though not always, these jets have a strong helical flow component. A relationship between bright points, jets, and the diffuse, persistent columns known as coronal plumes has long been suspected, but has proven difficult to verify and explain. Thus far the strongest connection appears to be the existence of tiny "jetlets" observed within some plumes (Raouafi et al. 2008; Raouafi & Stenborg 2014), but it is unclear whether all plumes are composed of many such impulsive events or whether a different mechanism (e.g., weak, quasi-steady null-point reconnection) is responsible for the enhanced density and flows of plumes.

On close inspection, CH jet sources and anemone-type bright points (e.g., Galsgaard et al. 2017) match the magnetic

topology of an embedded bipole: a three-dimensional (3D) coronal magnetic null point, with associated inner and outer spine lines and a fan separatrix surface (Antiochos 1990; Lau & Finn 1990). The photospheric manifestation of this configuration is a minority-polarity intrusion within the majority-polarity magnetic field. The fan surface separates the closed magnetic flux beneath the null point from the globally open flux above and away from the null point. Relative motions of the two flux systems can readily distort the null to form a current sheet there (Antiochos 1996), setting the stage for interchange reconnection between open and closed field lines and associated plasma flows and heating. It is broadly accepted that coronal jets are driven by the onset of explosive magnetic reconnection, while some observational studies have speculated that more gradual reconnection in the same magnetic structure could explain a long-duration bright point (e.g., Doschek et al. 2010; Pucci et al. 2012; Zhang et al. 2012).

In previous work, we and our colleagues have investigated the generation of CH jets within the embedded-bipole model and its null-point topology. The essential feature needed to generate an explosive jet in this model is to store a substantial amount of magnetic free energy within the low-lying closed flux. In configurations with a nearly uniform majority-polarity background field, twisting the internal closed flux by imposing slow, quasi-circular surface flows eventually leads to the onset of a kink-like instability. Strong feedback between the ideal triggering mechanism and rapid reconnection through the null-point current sheet releases much of the stored free energy and generates a helical, Alfvénic jet (Pariat et al. 2009, 2010, 2015, 2016; Wyper & DeVore 2016; Wyper et al. 2016; Karpen et al. 2017). In more recent work, we investigated cases that have a strong majority-polarity concentration adjacent to the minority-polarity intrusion. In that case, a filament channel of strongly sheared, low-lying magnetic flux forms at the polarity inversion line (PIL) between the two concentrations. Reconnection above the PIL forms a flux rope that can support a mini-filament, which rises slowly and eventually erupts as a jet through reconnection between the flux rope and the external field (Wyper et al. 2017, 2018). The underlying mechanism is an exact analog to the breakout model that explains fast coronal mass ejections (CMEs; Antiochos 1998; Antiochos et al. 1999).

Our preceding jet modeling assumed photospheric rotational motions that were strictly internal to the closed-field region. Consequently, we obtained two types of reconnection-driven outflows: weak intermittent plasma releases and energetic helical jets accompanied by transient bright points beneath the domed separatrix. In this paper, we study the activity driven by larger scale, linear footpoint motions that transport the minority-polarity intrusion across the solar surface, as occurs with MMEs in CHs. Specifically, we consider the scenario when this motion subjects the closed field beneath the separatrix to a broad shear. We have investigated three configurations of increasing complexity and activity. In the first, the minority-polarity flux was moved quite uniformly, but part of the surrounding majority-polarity background flux was left behind due to a gradient in the imposed surface flow. The separatrix was distorted by this shear flow, inducing the development of currents and low-intensity reconnection at the null point. We show that the reconnection process has a natural periodicity, reminiscent of a bright point with quasi-periodic intensity fluctuations. In the second configuration, the minority-polarity patch was placed closer to the gradient in the imposed photospheric flow, so that the flux was substantially sheared and the surrounding PIL was strongly distorted. This case exhibited elevated reconnection and explosive jetting. It transitioned between long-duration, low-intensity bright-point-like reconnection and short-duration, high-intensity jet-like reconnection and back again. Third, we added a concentration of majority-polarity flux to the second configuration, then advected the minority- and new majority-polarity concentrations past one another. This "flyby" configuration produced still more energetic and explosive activity as the MMEs first connected to, then disconnected from, each other as they passed.

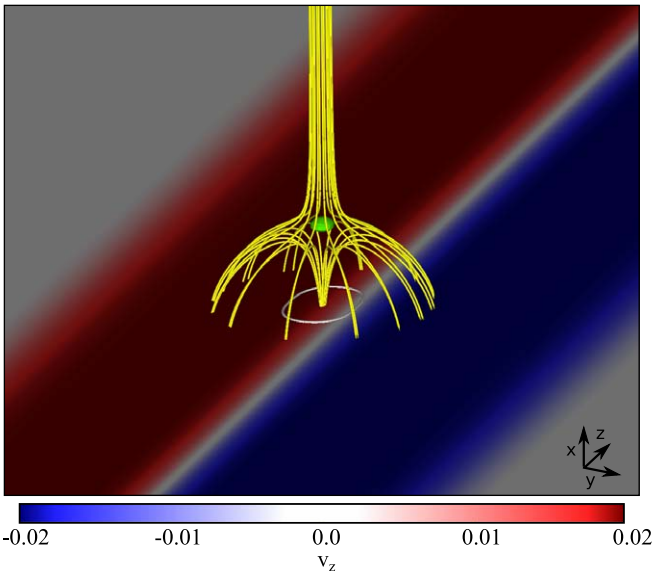

Figure 1. The magnetic field and surface flow profile in configuration 2. Yellow field lines depict the spine-fan topology of the field above the minority polarity. The green sphere is an isosurface of plasma $\beta = 10$, showing the position of the null point. The PIL is shown as a white contour. Color shading on the surface shows the magnitude and sign of v_z.

In Sections 2 and 3, we describe the simulation setup and the diagnostics used to interpret the results. The simulations and our analyses are presented in Section 4. We demonstrate good quantitative agreement between our results and observations, and discuss the implications of our work for natural links between bright points, CH jets, and plumes, in Section 5. In Section 6, we briefly list the major conclusions of this work.

2. Setup

We set up a simple system consisting of a single minority-polarity (positive) concentration embedded in a majority-polarity (negative) background. Figure 1 shows the magnetic field (yellow lines) above the minority polarity in one of the simulations. The field has the typical fan-spine null-point topology associated with an embedded minority polarity (e.g., Antiochos 1996). Also shown are the surface polarity inversion line (white contour) and a unidirectional imposed flow (color shading) on the surface. For maximum generality, we conducted our experiments in nondimensionalized units. As discussed below, the results can be scaled to physical units by applying appropriate solar scale factors to the nondimensionalized results.

We constructed the minority polarity by superposing five vertically aligned, subphotospheric magnetic dipoles, such that

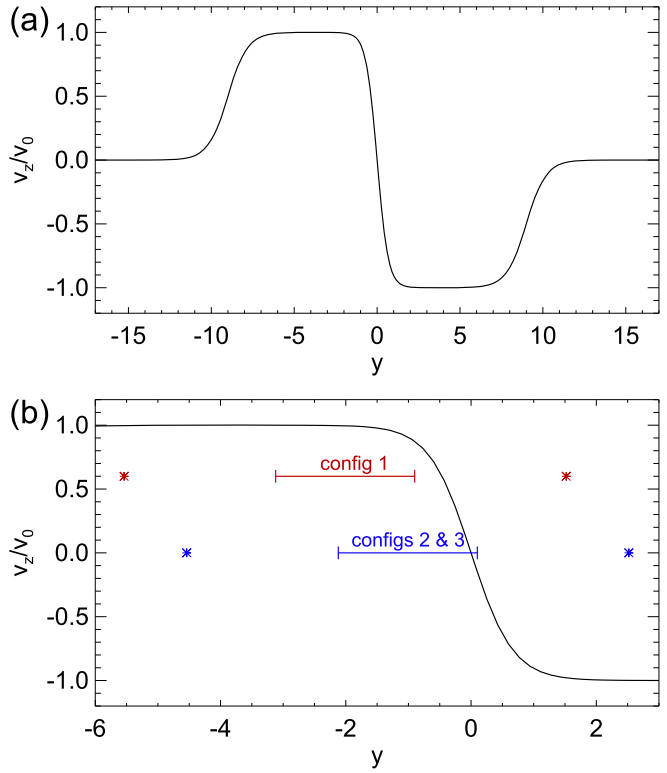

Figure 2. (a) Normalized surface flow profile. (b) Zoom-in of panel (a) near the minority-polarity patch. Blue and red lines show the position and y extent (bounded on the left and right by the PILs) of the minority-polarity patch, and asterisks show the y extent of the separatrix footprint, for configurations 1, 2, and 3.

the initial potential field $\boldsymbol{B}$ and vector potential $\boldsymbol{A}$ are given by

$$\boldsymbol{B} = (b_0, 0, 0) + \sum_{i=1,5} \boldsymbol{\nabla} \times \boldsymbol{A}_i, \tag{1}$$

$$\boldsymbol{A}_i = \frac{b_i\,|x_i|^3}{2[x_i'^2 + y_i'^2 + z_i'^2]^{3/2}}[-z_i'\hat{\boldsymbol{y}} + y_i'\hat{\boldsymbol{z}}], \tag{2}$$

where $x_i' = x - x_i$, $y_i' = y - y_i$, and $z_i' = z - z_i$. We set $b_0 = -1.0$, $b_i = 11.0$, and $x_i = -1.0$ in all simulations. The five dipoles are placed on a line along the z direction from $z_i = -7.0$ to $z_i = -5.0$ at intervals of $\Delta z_i = 0.5$. $y_i = y_0$ is a fixed constant that controls the separation between the center of the minority-polarity concentration ($y = y_0$) and the center of the surface flow profile ($y = 0$).

The surface flow is given by

$$v_z = \begin{cases} \frac{v_0}{2}\left(\tanh\left(\frac{5(y+9)}{6}\right) + 1\right), & -17 \leqslant y < -5; \\ -v_0 \tanh\left(\frac{3y}{2}\right), & -5 \leqslant y < 5; \\ \frac{v_0}{2}\left(\tanh\left(\frac{5(y-9)}{6}\right) - 1\right), & 5 \leqslant y < 17; \\ 0, & 17 \leqslant |y|. \end{cases} \tag{3}$$

The profile is shown in Figure 2(a). Two bounded regions exist where the surface field is translated bodily along z in opposite directions. These are separated by a shear region of width $w \approx 3$ centered at $y = 0$. The driving profile is divergence-free, so that the surface magnetic flux is sheared as it is advected, but it is not canceled anywhere.

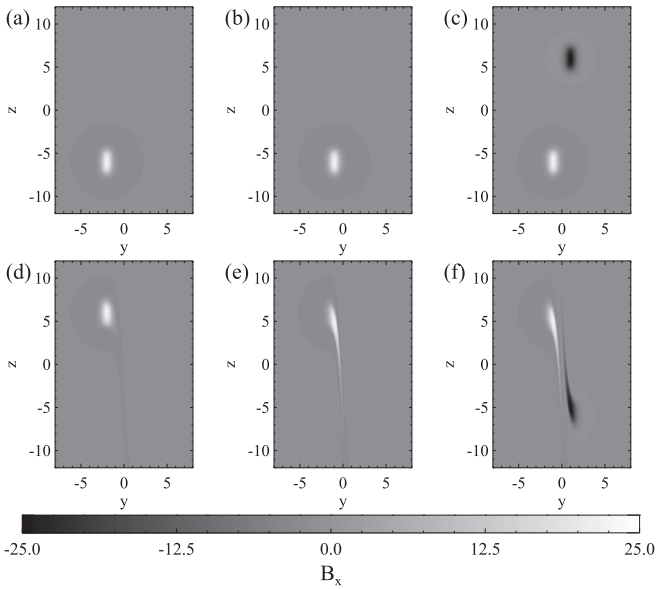

Figure 3. Surface B_x evolution in the three configurations. Left panels: configuration 1. Middle panels: configuration 2. Right panels: configuration 3. Top row: $t = 0$, bottom row: $t \geqslant 650$ ($t \geqslant 1250$ for configuration 1S).

We studied three configurations that were expected to produce increasing levels of jetting activity. In configuration 1, we set $y_0 = -2.0$, which positions the minority polarity almost entirely within a region of uniform translational motion. This is illustrated by the red line in Figure 2(b), which indicates the extent of the PIL for this case. Nevertheless, the patch is close enough to the shear zone about $y = 0$ that some field lines emanating from the patch close down on the far side of the shear zone. The footprint of the separatrix surface, shown by the red asterisks in Figure 2(b), spans the shear region, so the separatrix is sheared directly by the flow. Configuration 1, therefore, represents an almost uniform advection of a minority-polarity MME through weak majority-polarity flux. The initial and final surface flux distributions for this case are shown in Figures 3(a) and (d).

For configuration 2, we set $y_0 = -1.0$, so that part of the PIL lies very close to the center of the shear zone. This is illustrated by Figure 1 and by the blue line in Figure 2(b). The minority-polarity patch itself is sheared strongly by the driving motions in this case, and free energy is injected deep into the closed-field region. Hence, configuration 2 represents strongly nonuniform advection of the minority-polarity MME. The initial and final surface flux distributions for this case are shown in Figures 3(b) and (e).

Configuration 3 is a modification of configuration 2 in which we added a strong patch of majority-polarity (negative) flux, equidistant from the center of the shear zone but in the region of oppositely directed flow. The majority-polarity patch is constructed from five dipoles like the minority polarity, but with $b_i = -11.0$, $y_i = +1.0$, and $z_i = +5.0$ to $z_i = +7.0$. It is advected towards and past the minority polarity by the large-scale flow. Configuration 3 thus presents a sheared "flyby" of two MMEs, minority and majority, as shown in Figures 3(c) and (f). We will demonstrate later that their interaction leads to increased jetting activity during the evolution, relative to configurations 1 and 2. Note that in spite of the extreme deformation of the initial flux distribution, as evident in

Figures 3(c) and (f), the normal flux of the minority polarity at the boundary ($\Psi_{pp} \approx 55.4$) was conserved to within 98%.

In all cases, we ramped up the flow over 50 time units, held it constant for a time, and then ramped it down to zero, again over 50 time units. The minority-polarity patch was advected from its centered starting position at $z = -6.0$ to $z = +6.0$ (Figure 3). We considered two flow speeds, slow (S) and fast (F), for configuration 1. Configuration 1S had a driving speed $v_0 = 0.01$ and required a total driving duration of 1250 time units, whereas configuration 1F had $v_0 = 0.02$ over a duration of 650 time units. In configurations 2 and 3, we applied only the fast flow of configuration 1F.

We used the Adaptively Refined Magnetohydrodynamics (MHD) Solver (ARMS; DeVore & Antiochos 2008) to solve the ideal MHD equations in the form

$$\frac{\partial \rho}{\partial t} + \nabla \cdot (\rho \boldsymbol{v}) = 0, \tag{4}$$

$$\frac{\partial (\rho \boldsymbol{v})}{\partial t} + \nabla \cdot (\rho \boldsymbol{v}\boldsymbol{v}) + \nabla P - \frac{1}{\mu_0}(\nabla \times \boldsymbol{B}) \times \boldsymbol{B} = 0, \tag{5}$$

$$\frac{\partial U}{\partial t} + \nabla \cdot (U \boldsymbol{v}) + P \nabla \cdot \boldsymbol{v} = 0, \tag{6}$$

$$\frac{\partial \boldsymbol{B}}{\partial t} - \nabla \times (\boldsymbol{v} \times \boldsymbol{B}) = 0, \tag{7}$$

where t is the time, ρ is the mass density, $P = \rho RT$ is the thermal pressure, $U = P/(\gamma - 1)$ is the internal energy density, $\mu_0 = 4\pi$ is the magnetic permeability, and $\boldsymbol{B}$ and $\boldsymbol{v}$ are the 3D magnetic and velocity fields. An ideal gas is assumed, with ratio of specific heats $\gamma = 5/3$. Similar to our previous jet experiments (e.g., Wyper & DeVore 2016; Wyper et al. 2018), we imposed an initially uniform plasma density, temperature, and pressure of 1.0, 1.0, and 0.01, respectively; hence, the nondimensional gas constant is $R = 0.01$. The corresponding plasma $\beta \approx 2 \times 10^{-1}$ in the background field, dropping to $\beta \approx 5 \times 10^{-4}$ at the surface within the minority polarity. The initially uniform sound speed $v_s \approx 0.13$, while the Alfvén speed varies from $v_a \approx 0.3$ in the background field to $v_a \approx 6.5$ in the minority polarity. The largest driving speed used in our simulations is 0.02, approximately 15% of the sound speed and 6.7% of the background Alfvén speed. Thus, the region around our MMEs evolved quasistatically in response to the imposed surface flow. Reconnection eventually occurred in all of our simulations due to inherent numerical diffusion during the time advancement of the MHD equations, in particular the induction equation for the magnetic field. This effective numerical magnetic diffusion is as small as possible for the given simulation grid while maintaining numerical stability and monotonicity (DeVore 1991).

When the driving began in the two counterpropagating flow regions, two large-scale Alfvén wave fronts propagated upwards into the simulation volume. The box size in each simulation is $[0, 192] \times [-32, 32] \times [-32, 32]$, tall enough that the disturbance from the driving profile reached the top boundary at $t \approx 680$. The simulations with $v_0 = 0.02$ were halted at about this time. Consistent with the boundary driving, periodic boundary conditions were applied to the z boundaries, while the side y boundaries were closed and line-tied. Open, zero-gradient boundary conditions were applied at the top boundary, except that the tangential velocity components were set to zero beyond the boundary to partially damp the slippage of field lines. Some of the Alfvén wave disturbance was reflected from this boundary in the case with $v_0 = 0.01$, where the driving was applied over a longer time. However, the simulation was halted before the reflections reached the jetting region at $t \approx 1360$. The bottom boundary was closed and line-tied everywhere. Except where the driving profile above was prescribed, the tangential velocity was zero.

The simulation grid was adapted dynamically and managed by the PARAMESH toolkit (MacNeice et al. 2000). It refined/derefined according to local measures of the gradient and strength of the magnetic field (see the Appendix in Karpen et al. 2012). In terms of the adaptive parameters introduced in Karpen et al. (2012), we used $c_1 = 0.01$, $c_2 = 0.04$, $B_1 = 1 \times 10^{-4}$, and $B_2 = 20$. These values were found to resolve the reconnection region and jet outflows well, and to track them as they propagated upwards into the simulation volume. We used five levels of grid refinement in these simulations, corresponding to a minimum grid spacing of 6.25×10^{-2}. Additionally, a subvolume large enough to encompass the separatrix surface as it was advected across the domain was fixed at the maximum refinement level throughout the simulations, to maximally resolve the dynamics around the MMEs.

For generality, the equations were solved in dimensionless form. Hence, the time units of the simulations can be understood relative to characteristic timescales of the system. The separatrix dome is ≈7 length units wide, while the Alfvén speed at the center of the minority polarity is ≈6.5 velocity units. Thus, a time unit of 1 corresponds roughly to the travel time of an Alfvén wave across the width of the separatrix dome. Our results can be scaled to solar observations by fixing a typical dome length scale (L_s), magnetic-field strength (B_s), and plasma density (ρ_s). Other useful quantities such as

$$V_s = \frac{B_s}{\sqrt{\rho_s}}, \quad t_s = \frac{L_s}{V_s}, \quad E_s = B_s^2 L_s^3 \tag{8}$$

that fix the velocity, time, and energy scales then can be deduced. For example, choosing $L_s = 2.5 \times 10^8$ cm, $B_s = 2.5$ G, and $\rho_s = 4 \times 10^{-16}\,\mathrm{g\,cm^{-3}}$ gives $V_s = 1250\,\mathrm{km\,s^{-1}}$, $t_s = 2$ s, and $E_s = 9.8 \times 10^{25}$ erg, yielding impulsive speeds, timescales, and liberated energies typical of coronal bright points and jets (see Section 5). For simplicity and generality, however, the values quoted below are given in nondimensionalized units.

3. Diagnostics

To investigate the reconnection process, we identified and tracked the positions of the null point (or cluster of null points) associated with the minority polarity using the trilinear method described in Haynes & Parnell (2007); for details of the implementation in ARMS, see the appendix of Wyper et al. (2016). As in that paper, we also identified the open–closed separatrix associated with the null (or nulls) by sampling the connectivity of points within the domain and assigning each point a functional value of $f(x, y, z) = 0$ in an open field region and $f(x, y, z) = 1$ in a closed field region. The separatrix was then visualized as an isosurface of $f(x, y, z) = 0.5$. Another informative reconnection diagnostic was the normalized interchange reconnection rate,

$$\frac{d\Psi}{dt}(t) \approx \frac{|\Psi_{\mathrm{opened}}| + |\Psi_{\mathrm{closed}}|}{2\Psi_{pp}\Delta t}, \tag{9}$$

where Δt is the time between simulation snapshots, $\Psi_{pp} \approx 55.4$ is the flux of the minority polarity, and $\Psi_{\rm opened}$ and $\Psi_{\rm closed}$ are the amounts of newly opened and closed flux, respectively, since the previous snapshot. Formally, $\Psi_{\rm opened}$ should equal $\Psi_{\rm closed}$, but numerically small variations exist so we take their average. To calculate $\Psi_{\rm opened}$ and $\Psi_{\rm closed}$, the ideal motions imposed at the boundaries must be filtered out. We do this by tracing field lines from a uniform grid on the photosphere at a given time to produce an array of field line end points, ($X_t(y, z)$, $Y_t(y, z)$, $Z_t(y, z)$). The same starting points are then advected by the boundary flow backwards in time to the previous snapshot (at $t - \Delta t$), whereupon field lines are traced from these positions at this time, giving a second set of field line end points, ($X_{t-\Delta t}(y, z)$, $Y_{t-\Delta t}(y, z)$, $Z_{t-\Delta t}(y, z)$). This second set is then advected forwards in time to the time of the original snapshot (t), whereupon they share the same starting positions as the original mapping, but preserve the connectivity of the previous time. Comparing the two mappings at time t, we identify newly opened and newly closed field lines over the time interval Δt (for an in-depth discussion, see Titov et al. 2009). Summing over all reconnected field lines, weighted by the magnetic flux at the field-line starting points, then gives $\Psi_{\rm opened}$ and $\Psi_{\rm closed}$ (for further details, see Wyper & DeVore 2016).

To investigate the energetics of our simulations, we calculated

$$K = \iiint \frac{1}{2}\rho v^2 \, dx \, dy \, dz, \tag{10}$$

$$M = \iiint \frac{1}{8\pi} B^2 \, dx \, dy \, dz, \tag{11}$$

the volumetric integrals of kinetic (K) and magnetic (M) energy, respectively. However, we found that the large-scale Alfvén wave disturbances launched by the boundary driving dominated the plots of these quantities, injecting large and sustained increases of kinetic and magnetic energy into the volume. In addition, the boundary shearing motions altered the surface flux distribution, changing the minimum-energy (potential) state of the magnetic field.

To minimize the Alfvén wave effect on the diagnostics, we ran reference simulations identical to each calculation but with the uniform background field only (i.e., omitting the subphotospheric dipoles) and calculated the energy associated with the large-scale Alfvén wave fronts. To account for the minimum-energy effect, we performed a potential-field extrapolation at each time using the evolved surface magnetic flux, thereby computing the changing baseline value of the magnetic energy. By subtracting these contributions from K and M, we estimated the kinetic energy (ΔK) generated by the reconnection outflows/jets and the free magnetic energy ($\Delta M_{\rm free}$) related to the stress in the closed-field region,

$$\Delta K = K - K_{\rm ref}, \tag{12}$$

$$\Delta M_{\rm free} = \Delta M - \Delta M_{\rm ref} - \Delta M_{\rm pot}, \tag{13}$$

where

$$\Delta M = M - M(t = 0), \tag{14}$$

$$\Delta M_{\rm ref} = M_{\rm ref} - M_{\rm ref}(t = 0), \tag{15}$$

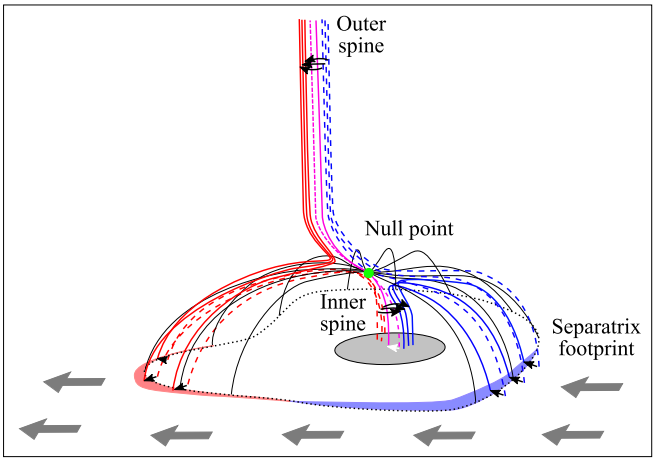

Figure 4. Schematic of the initial flux transfer process; see text for details. The fat gray arrows symbolize the surface flow in the reference frame of the moving minority-polarity element. The small black arrows indicate the direction of flux transfer: from dashed to solid across the separatrix and across/around the spine lines. The white arrow indicates the movement of the inner spine: from dashed to solid pink.

$$\Delta M_{\rm pot} = M_{\rm pot} - M_{\rm pot}(t = 0). \tag{16}$$

$M_{\rm ref}$ and $K_{\rm ref}$ are the kinetic and magnetic energy integrals calculated for the reference simulations, and $M_{\rm pot}$ is the magnetic energy of the potential field associated with the evolving surface flux at the simulation bottom boundary, all evaluated at time t. Note that $\Delta M_{\rm free}$ and ΔK are directly comparable, as $K_{\rm ref}(t = 0) = K(t = 0) = 0$, and the minimum state for kinetic energy is $K_{\rm pot} = 0$ at all times t.

4. Results

4.1. Configuration 1—Uniform Advection

In Configuration 1, the flow field was nearly uniform across the minority-polarity concentration, so that the closed field near the PIL was only weakly sheared. Part of the footprint of the separatrix surface, on the other hand, was significantly stressed by the driving motions. Consequently, we expect that a current layer will form readily around the magnetic null point due to the displacement of the inner (closed) and outer (open) flux systems, facilitating reconnection there (e.g., Antiochos 1996; Karpen et al. 1996; Pontin et al. 2007; Edmondson et al. 2010). The fields involved are relatively weak and large scale, and they accumulate little free energy, so the reconnection is not expected to be explosive. Instead, because the injected stress will continually propagate towards and be processed through the null point, we anticipate that the reconnection will involve only weak energy release and eventually establish a quasi-steady or quasi-cyclical evolution.

Figure 4 shows a schematic of this process in a frame of reference moving with the minority polarity. The minority-polarity region is shown in gray, with the PIL outlined in black. The green dot denotes the null point, while the solid black and solid/dashed magenta field lines show part of the fan separatrix and spine lines before and after reconnection, respectively. The thick gray arrows show the surface flows relative to the minority-polarity region. The action of the surface flows drags the separatrix out behind the minority polarity, distorting the footprint of the separatrix on the surface (black dotted line). This stresses the null-point region, collapsing the spine and fan

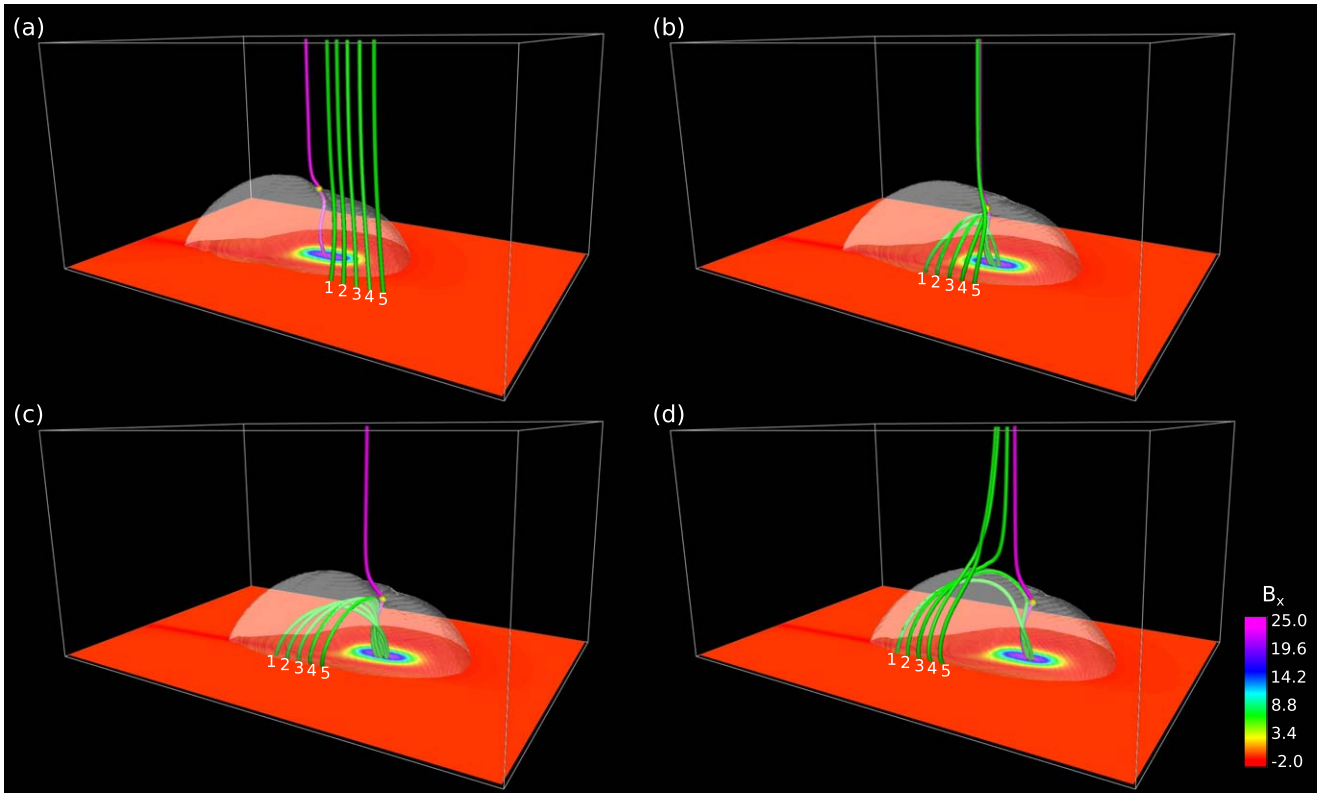

Figure 5. Field lines reconnecting during one cycle in configuration 1S. Semi-transparent isosurfaces show the separatrix, magenta field lines mark the spines and the yellow sphere is the null point. Green field lines are traced from footpoints on the surface that move along with the surface motions. Times are (a) $t = 590$, (b) $t = 770$, (c) $t = 870$, and (d) $t = 940$. An animation of this sequence is available. Its duration is 9 s.

(An animation of this figure is available.)

towards each other and forming a current layer around the null, even though the open outer spine is free to move. Reconnection within the current layer induces flux transfer across the separatrix, closing down the arriving flux (blue field lines, moving from dashed to solid) at the front of the separatrix and opening up the departing closed flux (red field lines moving from dashed to solid) at the trailing end of the separatrix. The shaded red and blue regions on the surface indicate the regions over which this flux transfer occurs.

Flux transfer in this manner is precisely what we see at the start of our simulation of configuration 1 and is similar to that found in previous investigations of null-point reconnection (e.g., Edmondson et al. 2010; Masson et al. 2012; Pontin et al. 2013). Unlike these previous works, however, in our simulation, the driving produced a sustained deformation of the closed flux region and, consequently, continuous storage of free magnetic energy. In order for interchange reconnection to release this internal free energy, the null and separatrix must evolve so as to penetrate into the affected closed flux region, which generally requires more intense reconnection dynamics, similar to what is seen in the standard models for coronal jets. As with homologous jets, this continued driving of configuration 1 resulted in cycles of energy buildup due to the ideal stressing and rapid release by reconnection.

One such reconnection cycle is shown from two viewpoints in Figures 5 and 6. The green field lines are traced from footpoints on the surface that move with the driving flows and are sequentially reconnected (from 1 to 5) into the minority polarity at the front of the separatrix (semi-transparent isosurface) as the cycle begins. Note that the associated newly opened field lines at the back of the separatrix are omitted for clarity. As the green field lines are reconnected at the null, the field lines are connected sequentially on the parasitic-polarity patch. Each new connection is made farther away from the leading edge of the separatrix than the last one. At the same time, the inner-spine footpoint follows these connections and is shifted backwards across the minority polarity (Figures 6(a) and (b)). As the driving continues, the surface motions drag the other footpoint of each field line past the minority polarity, folding the first field lines to be reconnected underneath the later ones and introducing a half turn of twist within this region (Figures 5(b) and (c)). The slight increase in magnetic pressure associated with the newly closed flux compresses the underside of the null as it passes the minority polarity, changing the angle of the current layer around the null. Consequently, flux begins to open all along the side of the separatrix closer to the center of the domain, shifting the inner-spine footpoint sideways (Figure 6(c)). A burst of reconnection occurs when this magnetic flux reaches the trailing edge of the separatrix surface, whereupon the inner-spine footpoint moves back to where it started (Figure 6(d)) as the closed field lines reconnect again in reverse order (Figure 5(d)). In the animation accompanying Figure 5, a whip-like relaxation of the last field lines to open can be seen, accelerating plasma in the reconnection outflow (discussed further below).

Throughout the cycle, magnetic flux continually closed down at the front of the separatrix and opened at the trailing end; no reversal of the main reconnection direction occurred as in the so-called "oscillatory reconnection" scenario (e.g., Craig & McClymont 1991; Thurgood et al. 2017). Rather, reversals

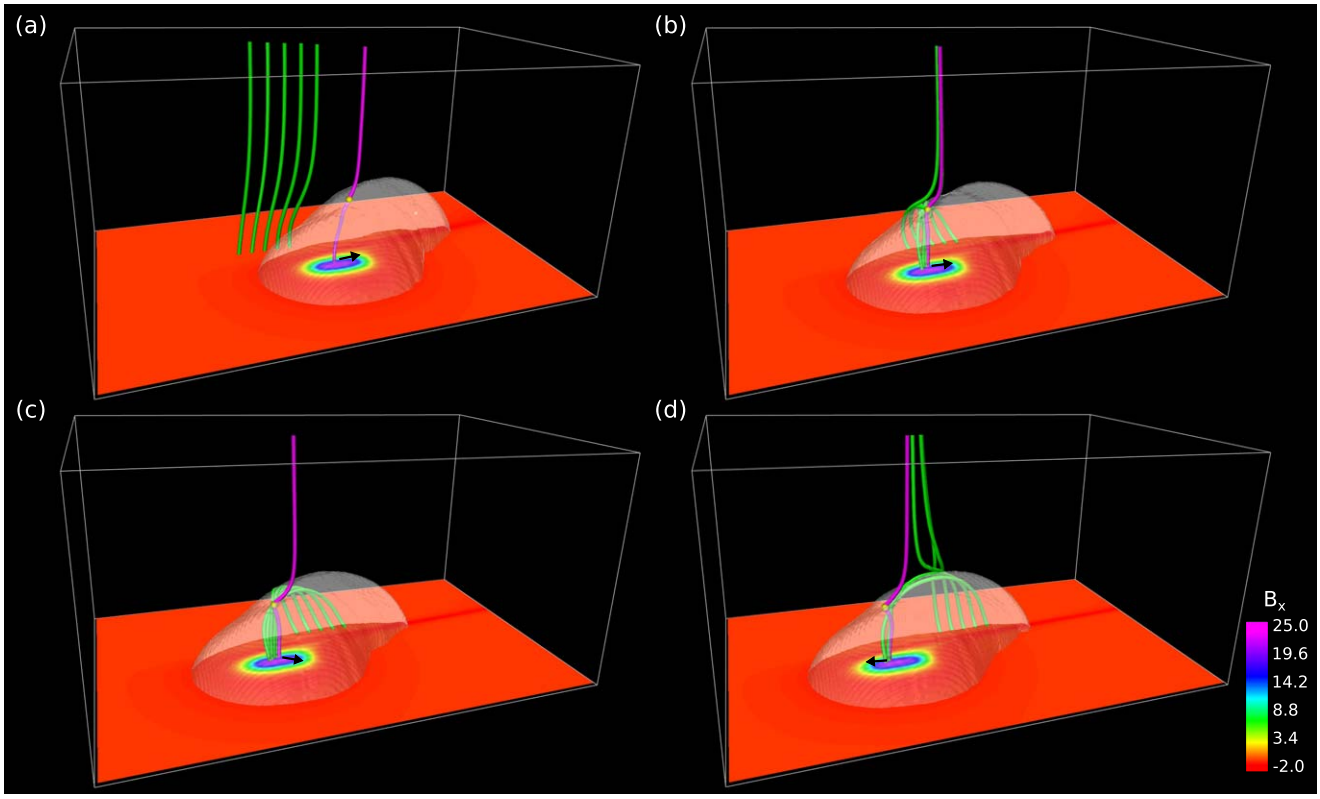

Figure 6. Movement of the footpoint of the inner spine during one cycle in configuration 1S. Quantities and times shown are the same as in Figure 5, but viewed from the opposite side of the domain. The black arrows indicate the instantaneous direction of motion of the inner spine. An animation of this sequence is available. Its duration is 9 s.

(An animation of this figure is available.)

of flux transfer took place along the sides of the separatrix. One such reversal is shown in Figures 7(a)–(d), which display the connectivity of the surface flux at various times during the same cycle. The flux transfer on the lower-right side varies from blue to red (closing to opening) and back again, while the front and back of the separatrix surface show continuous closing (blue) and opening (red) of flux, respectively. Additionally, the lower-left side of the separatrix also undergoes the opposite flux reversal to the right side (red to blue and back again) to preserve the net flux that is opened/closed.

Along with the footpoint of the inner spine, the null point also precessed in a circle as the closed-field evolution changed the stresses around the null. On top of this periodic motion, the null reconnection region was also slightly fragmented, which added some unsteadiness to the outflows and intermittently replaced the original null point with a small cluster of null points. To focus on the cyclic behavior, we show the position of the null point centroid (the average position of all nulls at a given time) after smoothing in Figure 8(a). The periodicity of its position as the minority polarity moved in the positive z direction is somewhat evident. However, when we shift to a frame of reference where the minority polarity is stationary ($z \rightarrow z^*$), the cyclic change in the null position becomes clear (Figures 8(b) and (c); see also the animation of Figure 7).

The duration and frequency of the reconnection cycles are displayed in Figure 9, which shows the peak current in the current layer, $J_{\max}$ (evaluated for field strengths where $B \leqslant 2.0$ to discount high volumetric currents), the peak plasma velocity in the volume, $V_{\max}$ (equivalent to the Alfvénic reconnection outflow velocity close to the current layer), the interchange reconnection rate, $d\Psi/dt$, and the position of the null in the moving coordinate system, z^*. Although the peak plasma velocity was significantly higher than the eventual outflowing plasma speed along the open field lines, which is closer to the local sound speed, it remains a useful indicator of the presence of reconnection-driven flows.

Following a ramp-up phase ($t \leqslant 250$), the system underwent three clear reconnection cycles and the start of a fourth before the driving began to ramp down at $t = 1200$. In each cycle, roughly the same changes in each quantity occurred, with peaks in current density and reconnection rate followed shortly thereafter by a peak in plasma velocity caused by a burst of outflow and a forward shift of the null position. However, significant variations among cycles are evident, as the burst of reconnection does not produce a simple reproducible evolution in which each cycle brings the system back to its initial pre-stressed state. The interchange reconnection rate and the peak current around the null evolved differently, as flux is transferred across the current sheets spanning the separatrix, not just at the null itself (e.g., Pontin et al. 2005; Wyper et al. 2012). Variations in the interchange reconnection rate slightly precede the corresponding variations in the peak plasma velocity, because the plasma is not instantaneously accelerated by the Lorentz force of newly reconnected field lines. The final outflow burst, shown in Figures 7(g) and (k), formed a narrow plasma spire that was denser and faster than the preceding quasi-steady reconnection flows. A similar spire formed during each cycle, seen clearly in the animation of the figure.

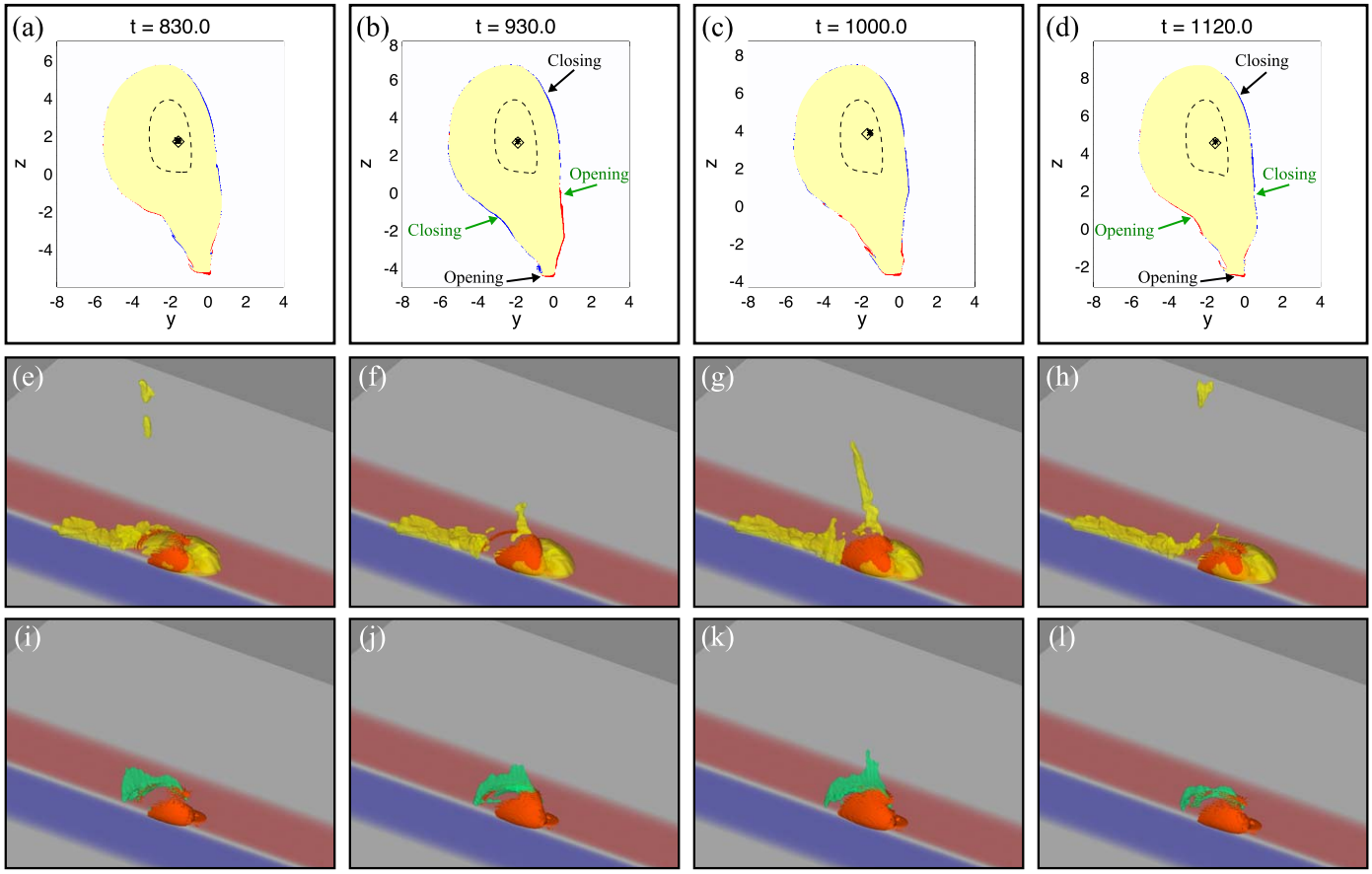

Figure 7. Configuration 1S: outflows and reconnected flux during one cycle. Top panels illustrate the connectivity of magnetic flux on the photosphere at the times indicated. White denotes open-field regions, yellow closed-field regions. Blue and red show flux that has recently closed and opened, respectively. The PIL is shown as a dashed line. Asterisks show the projections of the null point positions, while the diamond marks the position of the null point centroid (smoothed in time). Middle and bottom panels show the enhanced mass density (yellow isosurface, $\rho = 1.1$) and plasma velocity (green isosurface, $v = 0.05$), respectively, in the reconnection outflows. Orange isosurfaces show enhanced current density ($J = 0.3$). Red/blue shading shows the surface plasma velocity v_z; color scale as in Figure 1(b). An animation of these panels is available. The animation also shows the evolution of the parameters shown in Figure 9. The video begins at $t = 0$ and runs to $t = 1340$. The duration is 11 s.

(An animation of this figure is available.)

Thus, our results indicate that when minority polarity intrusions move relative to a weak background field such that the separatrix and some of the closed flux, but not the PIL, are sheared, the interchange reconnection at the null point is characterized by quasi-periodic weak bursts. Each burst arises from a cyclic closing and opening of flux as the minority polarity traverses the background field. We expect such quasi-steady reconnection to continually heat the closed loops along the driven side of the separatrix. Observationally, this should produce a bright-point signature, while the periodic bursts might be observed as periodic increases in intensity (see Section 5).

In the configuration 1 simulation, the system adapted to accommodate the rate at which flux is delivered to/removed from the reconnection region by the surface flows. Therefore, the cyclic reconnection dynamics and the assumed intensity modulation may be sensitive to the speed of the moving minority polarity, and also to the efficiency with which the reconnection region can process the arriving magnetic flux. To understand the nature of this relationship, we repeated the experiment with twice the surface driving speed. The driving in this case began to ramp down at $t = 600$, stopping at $t = 650$, so that the minority polarity was advected the same distance.

Figure 10 shows the same quantities for this configuration, 1F, as in Figure 9 for 1S. After a ramp-up phase ($t \leqslant 125$), three cycles of reconnection occurred (seen most easily in the peak current density), with the third continuing beyond the end of the driving period. Compared with configuration 1S, the increased driving speed and reconnection rate of configuration 1F yielded faster and more extended outflows (Figure 11).

As occurred with the slow driving, the cycles varied in length, with the middle being slightly longer and exhibiting more than one peak in $v_{\max}$. However, the 1F cycles were shorter by a factor of 1.5–2, similar to the difference in driving speed. This is the key result: for quasi-static driving, i.e., slow compared to the coronal Alfvén speed, the period of the reconnection cycles is set predominantly by the displacement of the minority polarity and not by an inherent timescale for the reconnection process. Again, this result is similar to what has been found in studies of homologous jets. A burst of reconnection and energy release occurs only after a sufficiently large amount of free energy has built up to trigger some type of feedback between the reconnection and the resulting global dynamics. Since actual photospheric driving velocities are a much smaller fraction of the coronal Alfvén speed than those adopted in our simulations, we expect that the cycle period is determined mainly by the flow speed on the Sun as well. In our

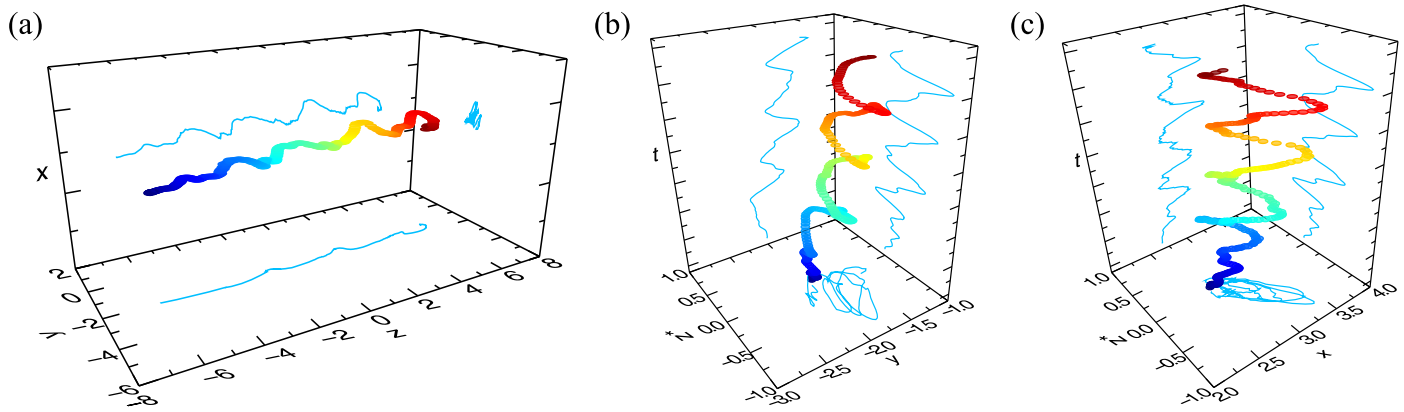

Figure 8. Smoothed evolution of the null-point centroid in configuration 1S. (a) 3D visualization and 2D projections of the evolving null position. Time increases from dark blue ($t = 0$) to dark red ($t = 1350$). Note the periodic change of position in y and x. (b) Rotation of the centroid in y and z about a central point moving with the flow. The vertical axis is time, and z^* is the z variation in the moving coordinate system. (c) Same plot but for x vs. z^*.

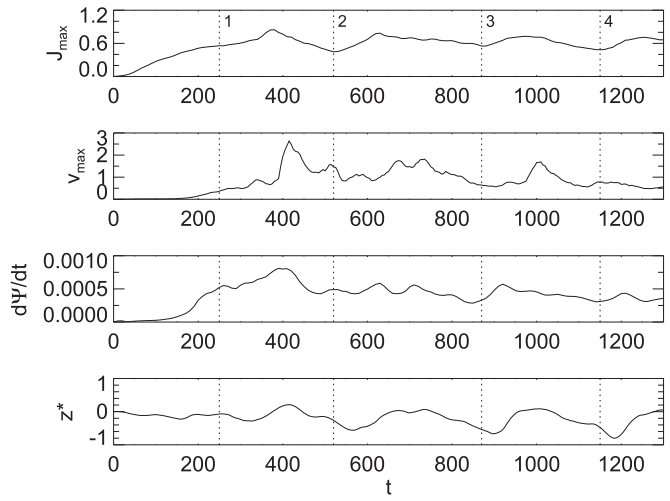

Figure 9. Configuration 1S. J_{max}, v_{max}, $d\Psi/dt$, and z^*, the location of the null centroid along the z direction relative to the moving coordinate system. Vertical dotted lines roughly delineate four cycles of energy buildup and release. All quantities have been smoothed.

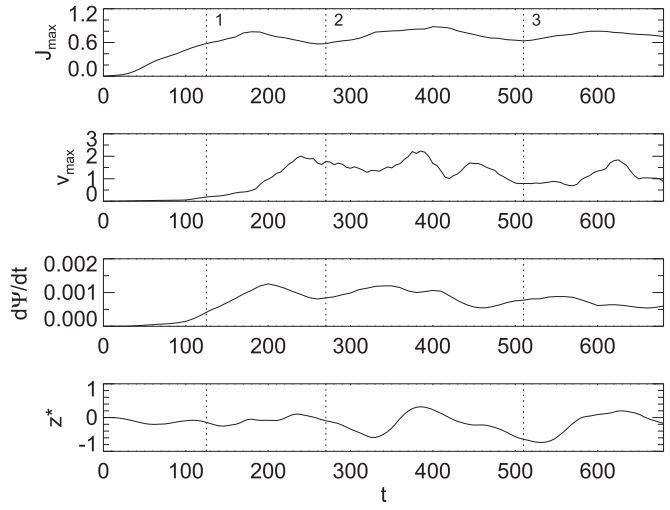

Figure 10. Configuration 1F. J_{max}, v_{max}, $d\Psi/dt$, and z^*, the motion of the null centroid in the z direction relative to the moving coordinate system. Vertical dotted lines roughly delineate three cycles of energy buildup and release. All quantities have been smoothed.

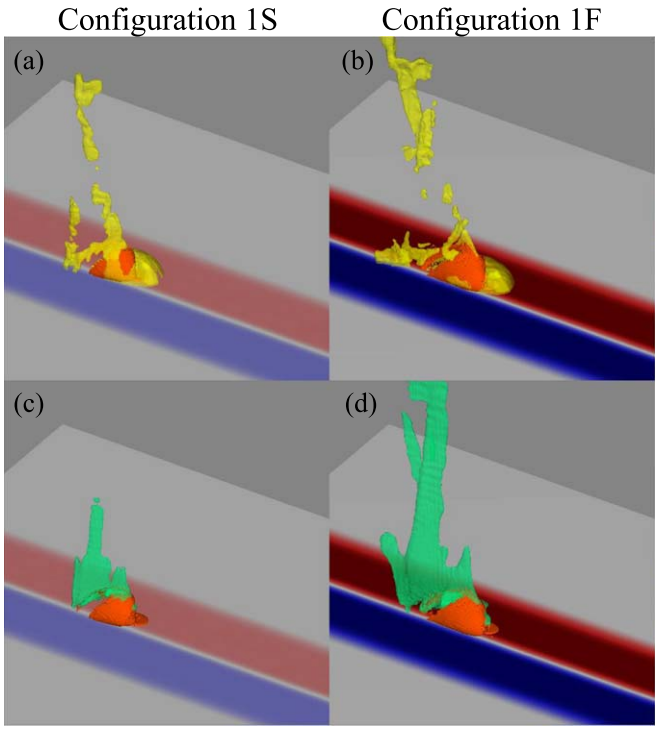

Figure 11. Comparison of the jetting/outflows at $t = 360$ in the two simulations for Configuration 1. Top panels: enhanced mass density ($\rho = 1.1$, yellow isosurfaces). Bottom panels: plasma velocity ($v = 0.05$, green isosurfaces). Orange isosurfaces show current density ($J = 0.3$). Red/blue shading shows the surface plasma velocity v_z; color scale as in Figure 1(b).

simulations, the minority polarity was displaced by a distance $D \approx 12$, approximately three times the length of the minority polarity patch ($d \approx 4$). Thus, a full cycle occurs every time the minority polarity is advected roughly its length across the solar surface. This is consistent with the picture presented in Figures 5 and 6 of flux opening along the side of the separatrix in a burst.

4.2. Configuration 2—Strong Shear

In configuration 2, the flow field was highly nonuniform across the minority-polarity concentration, so that the closed

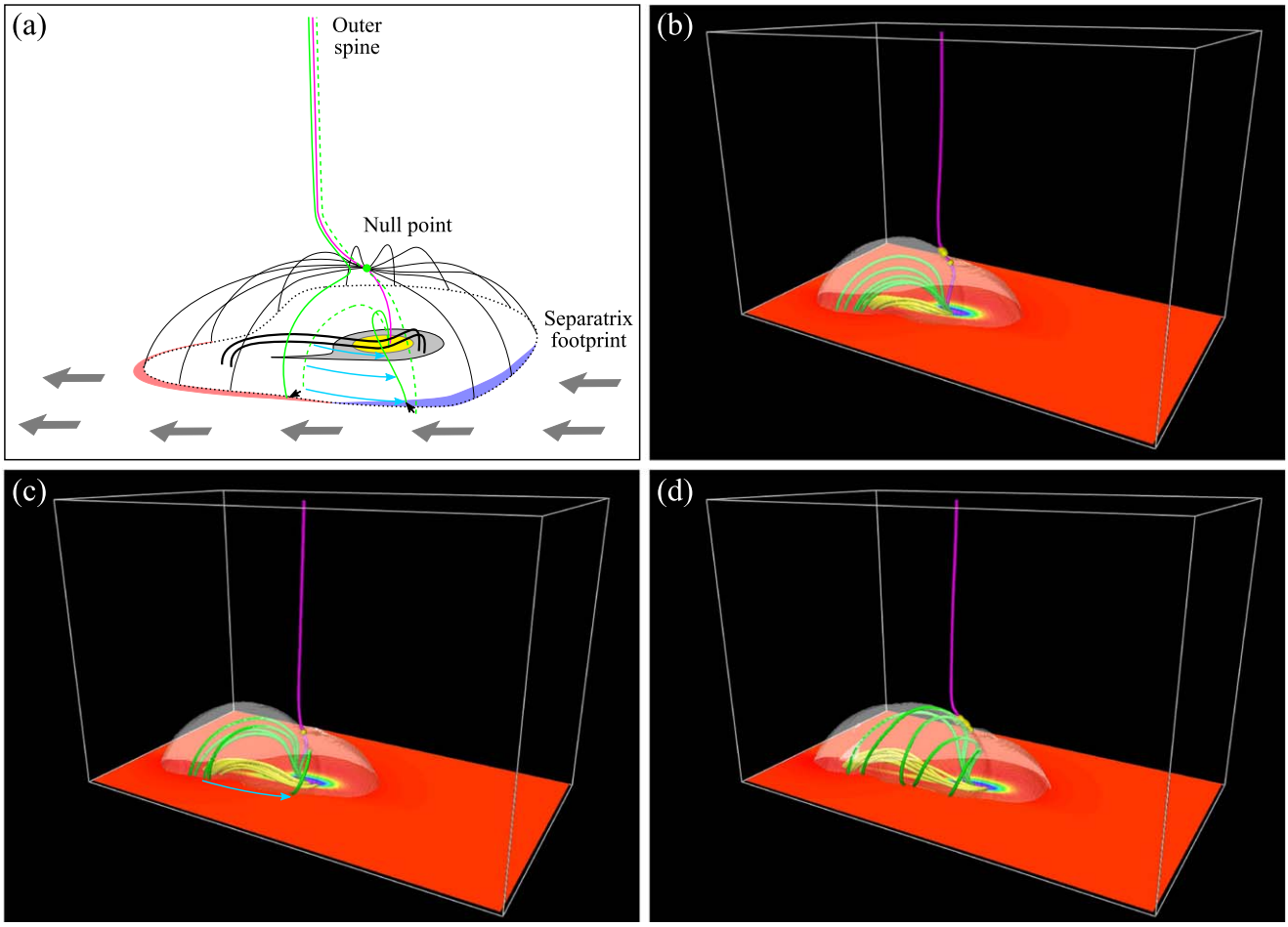

Figure 12. (a) Schematic of the initial filament-channel formation process in configuration 2. See the text for details. (b)–(d) Formation of the first filament channel ($t = 180$, 210, and 270, respectively). Filament-channel field lines are shown in yellow, strapping field lines in green (traced from footpoints in the minority polarity), and field lines near the spine(s) of the null(s) in magenta. Yellow spheres denote the null positions and the semi-transparent isosurface shows the separatrix. Surface shading of B_x is the same as in Figure 5.

field near the PIL was strongly sheared. This is a crucial difference from configuration 1. The cyclic reconnection described above affects only flux somewhat near the separatrix and the inner-spine footpoint; it does not reach the low-lying field near the PIL. Therefore, in this simulation, the stress adjacent to the PIL continued to accumulate until a sheared-arcade filament channel was formed, as illustrated by Figure 12(a). The yellow patch shows the region of surface flux that is affected by the cyclic reconnection occurring at the null. Green field lines with footpoints in this region undergo interchange reconnection, during which some of their shear is transferred to an open field line and propagates away. The cyan arrows show the reduction in shear in one such interchange reconnection event, where the two dashed field lines reconnect to form the two solid field lines. In contrast, the thick black field lines with footpoints near the PIL and outside the yellow region stretch to form a sheared arcade. The weakly sheared, repeatedly reconnecting green field lines form an overlying strapping field that constrains the arcade. Figures 12(b)–(d) shows the filament channel forming in this manner in the simulation; the filament-channel field lines are yellow, whereas the overlying strapping field lines are green. This leads to the intriguing result that, despite the relatively broad surface shear applied in the simulation, the system naturally forms a low-lying, highly sheared filament channel localized to the PIL, because quasi-steady interchange reconnection at the null continually relaxes the strapping field above.

Eventually, however, the sheared field of the filament channel builds up sufficient free energy to drive an explosive CME-like release. We identified two explosive eruptions in configuration 2 before the driving was halted. Figure 13 shows field lines in the erupting filaments in each case. The first filament (formed as described above) started out as a sheared arcade (Figure 13(a)), but as it began to rise, it was converted into a flux rope by closed–closed (tether-cutting) reconnection near the PIL. A jet was launched when the portion of the flux rope rooted in the majority polarity opened up by interchange reconnection at the current sheet surrounding the null, releasing the twist in this section as an Alfvén wave (Figures 13(b) and (c)). The portion of the flux rope rooted in the minority polarity remained closed but shifted to new, less sheared footpoints in the closed region, in a manner similar to the green field lines in Figure 12(a). This closed section formed the basis of the second filament (light blue field lines), which inherited the remaining twist/shear. Like the first filament channel, this second channel grew in length as the driving continued until eventually it too erupted, generating the second jet.

These eruptions proceeded in the same way as the breakout jets introduced by Wyper et al. (2017, 2018). Figures 14(a)–(d) show the current density in a plane that cuts across the second

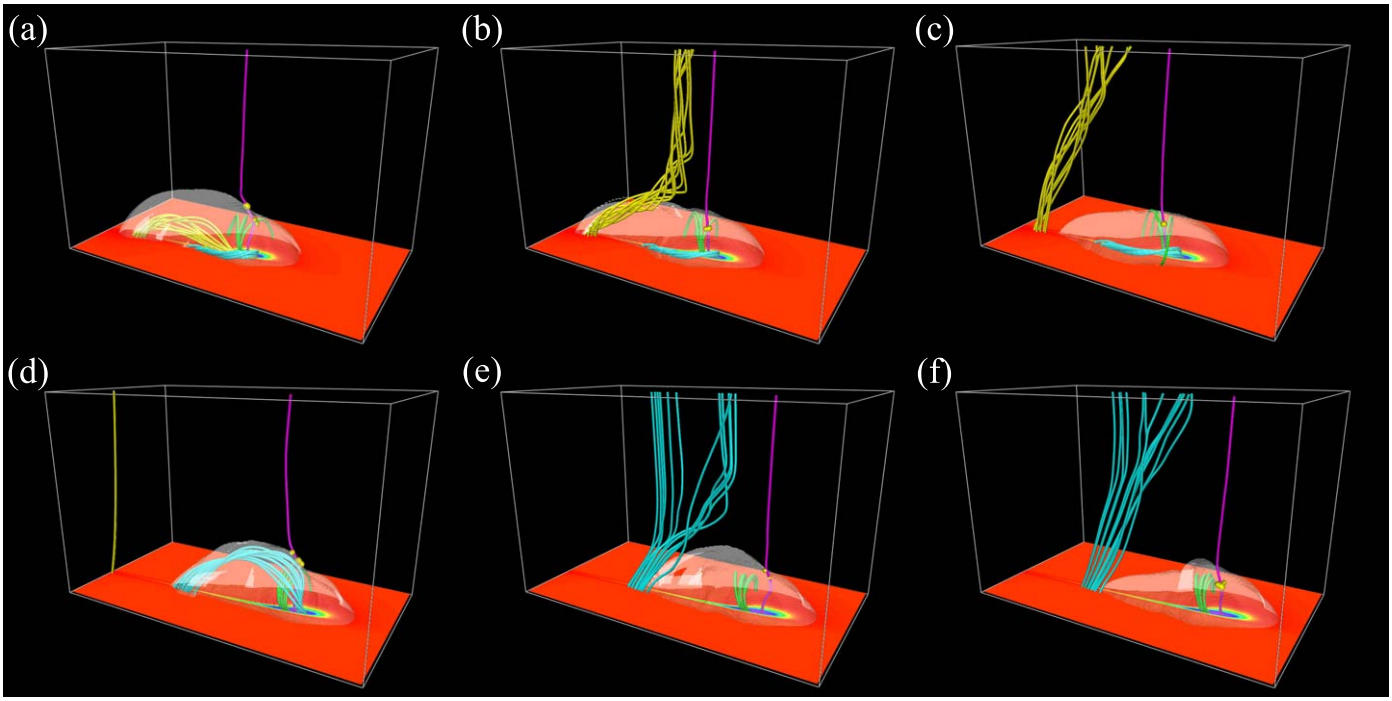

Figure 13. Two mini-filament jet eruptions in configuration 2. (a)–(c) First eruption ($t = 340$, 360, and 410). (d)–(f) Second eruption ($t = 550$, 570, and 590). The mini-filaments are drawn with yellow and light blue field lines, respectively. Shading, isosurfaces, and all other field lines as in Figure 12. An animation of this sequence is available. Its duration is 12 s.

(An animation of this figure is available.)

jet as the minority polarity moves, depicting the different phases of evolution. The plane is perpendicular to the section of the PIL along which the filament channel is aligned. Just prior to eruption onset (Figure 14(a)), the high volumetric current in the filament channel was visible on the right side of the separatrix dome (outlined by regions of medium strength current). By this stage, the strapping field mostly had been removed from above the filament by reconnection at the null, transferring flux to the unsheared side of the minority polarity and the open field, as shown by the white arrows. Thus, the null current layer acted as a breakout current sheet above the strapping field of the filament, releasing weak reconnection outflows (Figures 14(e) and (i)). The feedback between the rising filament and the reconnection at the null intensified the reconnection outflows as the filament rose (Figures 14(f) and (j)). Finally, a jet was launched when the filament reconnected across the breakout current layer (Figure 14(c)). At the same time, a flare current layer formed in the wake of the flux rope above growing post-flare loops (Figures 14(c) and (d)). Interestingly, the jet in this case does not exhibit much untwisting motion (Figure 14(l)), instead forming a narrow spire. Both straight and helical jets have been observed, with the latter more frequently associated with mini-filament eruptions (Moore et al. 2010; Sterling et al. 2015). We show a three-dimensional rendering of the current layers and plasma flows in our jet in Figure 15.

The jet signatures are prominent in the evolution of free magnetic ($\Delta M_{\rm free}$) and kinetic (ΔK) energy, shown in Figure 16, which also shows the change in potential energy ($\Delta M_{\rm pot}$) and the interchange reconnection rate ($d\Psi/dt$). For comparison, the same quantities for the other configurations are included. The nearly uniform advection applied to configuration 1 generated negligible outflow kinetic energy, while the free magnetic energy plateaued at a nearly constant value during each reconnection cycle. The two step increases in kinetic energy and dips in free magnetic energy (starting around $t = 330$ and $t = 550$) correspond to the onset of the two jets in configuration 2, as magnetic energy stored in the filaments was released via explosive interchange reconnection (Figure 16(d)) and converted to collimated plasma motion. Compared to the breakout jets studied by Wyper et al. (2017, 2018), in which about 50% of the stored magnetic energy was released during the jet, the fractional releases of magnetic energy (and the corresponding increases of kinetic energy) in these jets were significantly smaller. The main difference is that the filament was much smaller in the present simulations than in our previous simulations, straddling only a part of the PIL around the minority polarity rather than wrapping almost entirely around it. Smaller filaments store less free energy, so the resulting jets are less energetic, have narrower spires, and less observable rotation.

As with our earlier breakout-jet simulations, some magnetic shear remained behind within the filament channel after the jet was launched. This shear provided the foundation of the next filament channel, which formed as the surface motions continued to stress the closed-field region, leading to multiple eruptions. Indeed, these eruptions occurred on their own cycle, similar to the cyclic reconnection observed in configuration 1. During each breakout jet, the null point rotates around the separatrix from the breakout current layer to the flare current layer as the filament-channel field lines reconnect (Wyper et al. 2018). As the system begins to relax via flare reconnection and the post-flare loops build up, the null (along with its associated spine footpoint) then moves back to its initial position. We have confirmed this behavior in configuration 2 by tracking the evolution of the null centroid (not

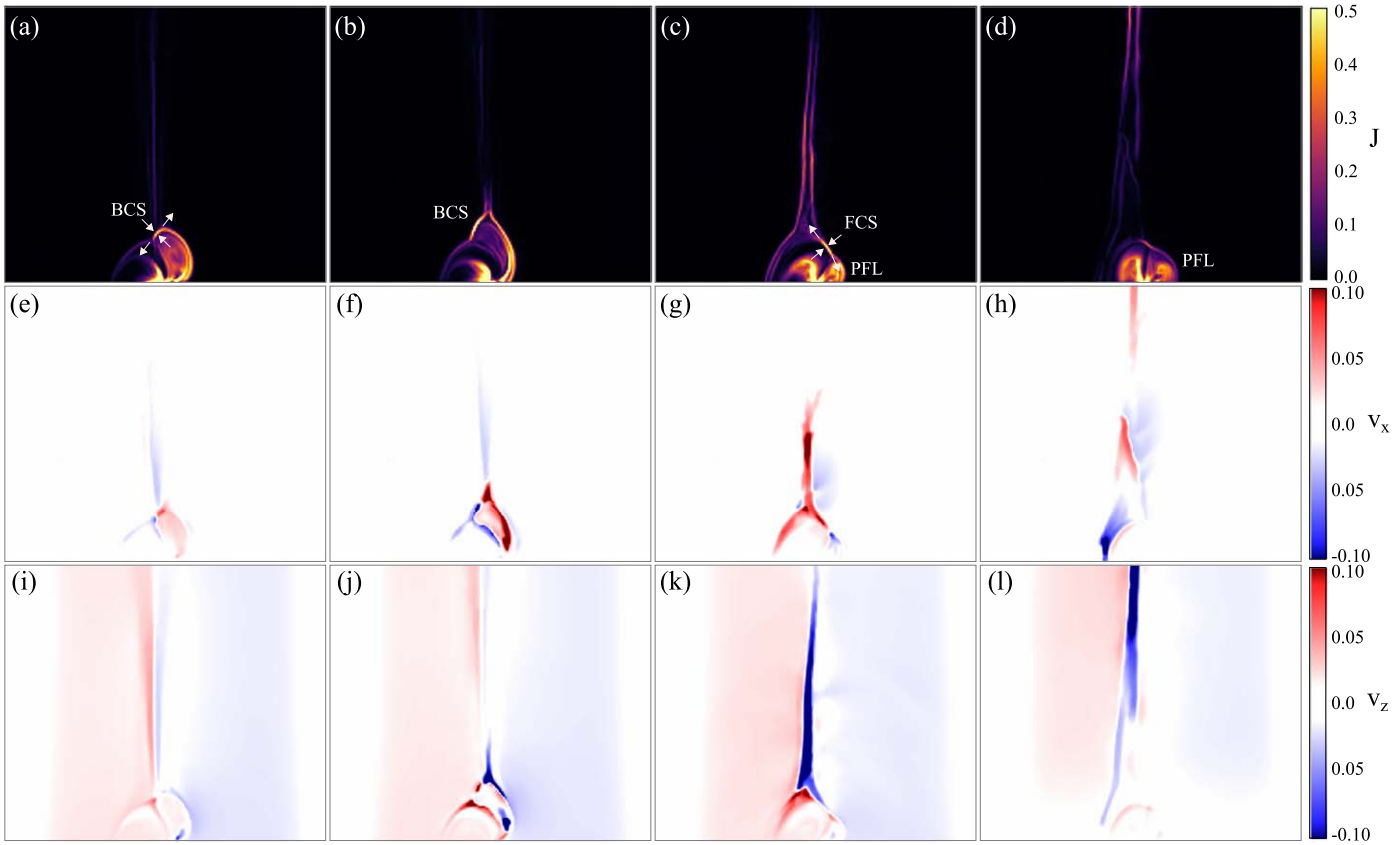

Figure 14. Current density J (top), v_x (middle), and v_z (bottom) in the $z = 1.92$ plane during the second jet in configuration 2. The panels are ordered from left to right corresponding to $t = 490$, 520, 580, and 610. Note that the minority polarity moves into the plane as viewed here. BCS = breakout current sheet; FCS = flare current sheet; PFL = post-flare loops. An animation of the top panels is available. Its duration is 9 s.

(An animation of this figure is available.)

shown). In this sense, each jet is simply an extension of the cyclic reconnection scenario of configuration 1, but with additional reconnection within the closed-field region to form and eject the flux rope.

This simulation demonstrates that when the field near the PIL of the minority polarity is strongly sheared, complex structure is created inside the separatrix through a combination of interchange (open/closed) reconnection at the null and tether-cutting (closed/closed) reconnection near the PIL. We expect both the overlying loops and the plasma within the filament channel to be heated. This might explain the more complex structure of some bright points observed in predominantly unipolar, open-field regions (e.g., Brown et al. 2001). Additionally, our simulation provides a link between jets and bright points, showing how the eruption of the filament channel explosively increases the interchange reconnection rate and generates a jet via the breakout mechanism.

4.3. Configuration 3—Flyby

In configurations 1 and 2, we assumed a perfectly uniform majority-polarity background field. However, the actual photospheric field is always clumped into locally strong concentrations. Increased activity is frequently observed when two or more such concentrations interact. We examined such encounters in configuration 3 by revising configuration 2 to include a strong concentration of majority-polarity flux. The majority intrusion was placed symmetrically with respect to the minority intrusion (Figure 17). As the two polarity concentrations were transported and sheared, they performed a flyby: approaching, passing, and then receding from each other during the encounter. Because the field above the majority polarity is more concentrated than the background, it expands laterally with height above the surface. Intuitively, we expect that the strong minority- and majority-polarity fields will preferentially establish transient connections as they pass each other. Such connections would be rife in the minimum-energy potential field, when the concentrated minority and majority polarities are closest. On the other hand, as the flyby finishes and the polarities recede from each other, we expect those connections to be undone. This preferential connection on approach, and disconnection on recession, is a central feature of the bright-point model of Longcope (1998).

Figure 18 compares the changing connectivity of the surface flux as the two concentrations passed one another (bottom panels) with the changing connectivity of configuration 2 (top panels). Before the majority concentration approached the minority, the flux connectivity was the same in the two cases (Figures 18(a) and (e)). As the majority polarity came closer, the connectivities began to differ, with connections forming quickly between the two flux concentrations in configuration 3. Figures 18(f) and (g) show that the background majority-polarity flux opened (red) along the top left of the separatrix when the flux of the majority-polarity concentration closed (blue) along the top right. This burst of interchange reconnection generated a second weak outflow at the front of the moving minority polarity, accompanying the ongoing quasi-steady

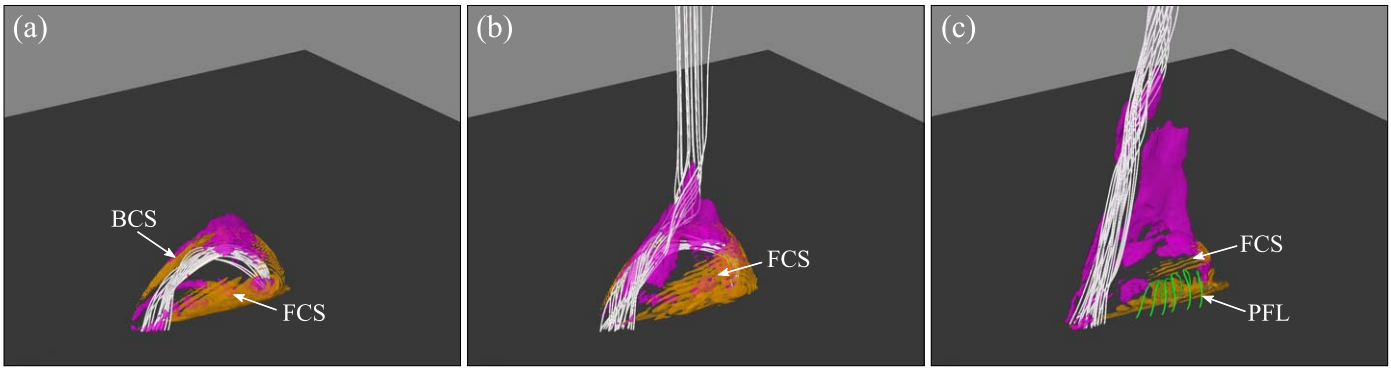

Figure 15. 3D rendering of the second jet eruption in configuration 3 at t = (a) 550, (b) 570, and (c) 600. Silver field lines depict the erupting filament. Isosurfaces show plasma velocity ($v = 0.15$, purple) and current density ($J = 0.6$, orange). BCS = breakout current sheet; FCS = flare current sheet; PFL = post-flare loops.

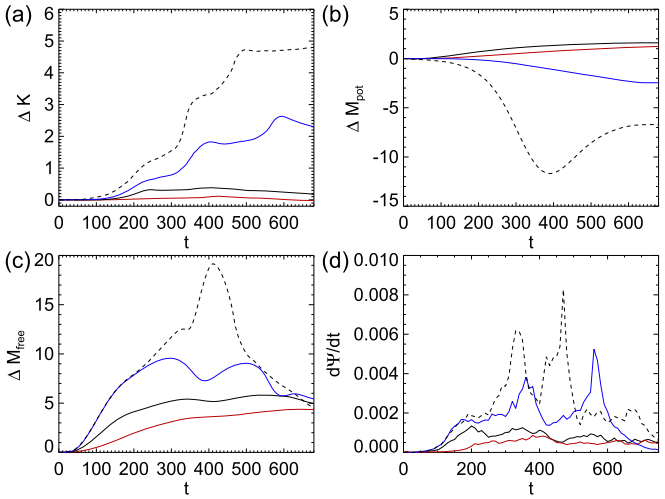

Figure 16. Simulation diagnostics. (a) Approximate kinetic energy of the outflows/jets. (b) Change in magnetic potential energy. (c) Approximate free magnetic energy. (d) Normalized reconnection rate. Solid red and black lines: configurations 1S and 1F, respectively. Solid blue: configuration 2. Dashed black: configuration 3.

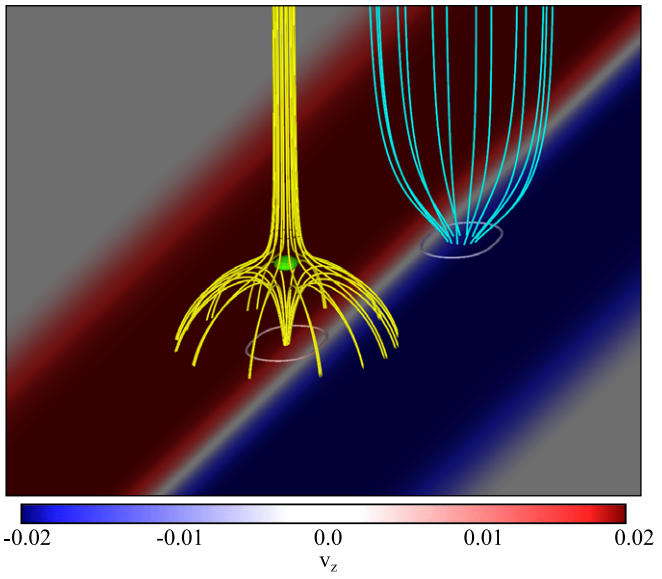

Figure 17. The magnetic field and surface flow profile in configuration 3. Yellow field lines, surface shading and isosurface as in Figure 1. Cyan field lines show the field curvature above the strong majority concentration of surface flux. The PIL is shown as a light pink contour. The light blue contour shows $B_x = -2.0$.

weak outflows from the rear of the separatrix (Figure 19(d); compare with configuration 2, panel 19(c)). The preferential connection to the flux of the passing concentration also shifted the null point away from the majority polarity as the flyby continued (Figure 18(h); see also the animation). This shift in the negative y direction changed the null position more than the cyclic motion induced by the jets.

Figure 16 shows the changes in energy during the flyby. Most notably, compared with the previous configurations, the potential energy of the system (dashed black line in Figure 16(b)) changed substantially, reaching a magnitude similar to the free energy injected by the driving (i.e., roughly equal to $\Delta M_{\rm free}$ in configuration 2, blue line in Figure 16(c)). $\Delta M_{\rm pot}$ dropped to its lowest value as the two polarity patches reached their closest approach, before increasing and finally saturating. This change reflects the connections formed between the two polarity regions, as if the opposing field components became superimposed and nullified each other within the volume as the two concentrations were brought closer together. In this sense, the start of the flyby is similar in some ways to a cancellation event in which the surface and volumetric fields are both canceled. The final $\Delta M_{\rm pot}$ is negative because the sheared tails of each polarity remained close to each other after the driving finished (Figure 3).

The reduction in the potential energy of the system led to substantially more free magnetic energy (Figure 16(c)). This free energy first became available when the two concentrations were close enough to interact (around $t = 200$), beyond which the curves of $\Delta M_{\rm free}$ diverge for configurations 2 and 3. The increased free magnetic energy drove more explosive, energetic jets in configuration 3. As in configuration 2, two main breakout jets were produced by bursts of reconnection (Figure 16(d)), causing stepped increases in kinetic energy (Figure 16(a)). Because the changing potential energy dominates the free magnetic energy in Figure 16(c), the drop in $\Delta M_{\rm free}$ during each jet manifests as a pause in the increase of $\Delta M_{\rm free}$ starting around $t = 330$ and a further steepening of the reduction in $\Delta M_{\rm free}$ (arising as the two patches move away from each other) starting around $t = 430$. A third small jet also occurred around $t = 680$, beyond the range of the energy plots but visible in the animation accompanying Figure 18. In comparison to configuration 2, the two main jets occurred in more rapid succession with higher reconnection rates and kinetic energy. However, unlike $\Delta M_{\rm free}$ and $d\Phi/dt$, the volumetric kinetic energy (ΔK) is higher than in configuration 2 even before $t = 200$ when the two polarities started to interact. The early increase follows from horizontal plasma

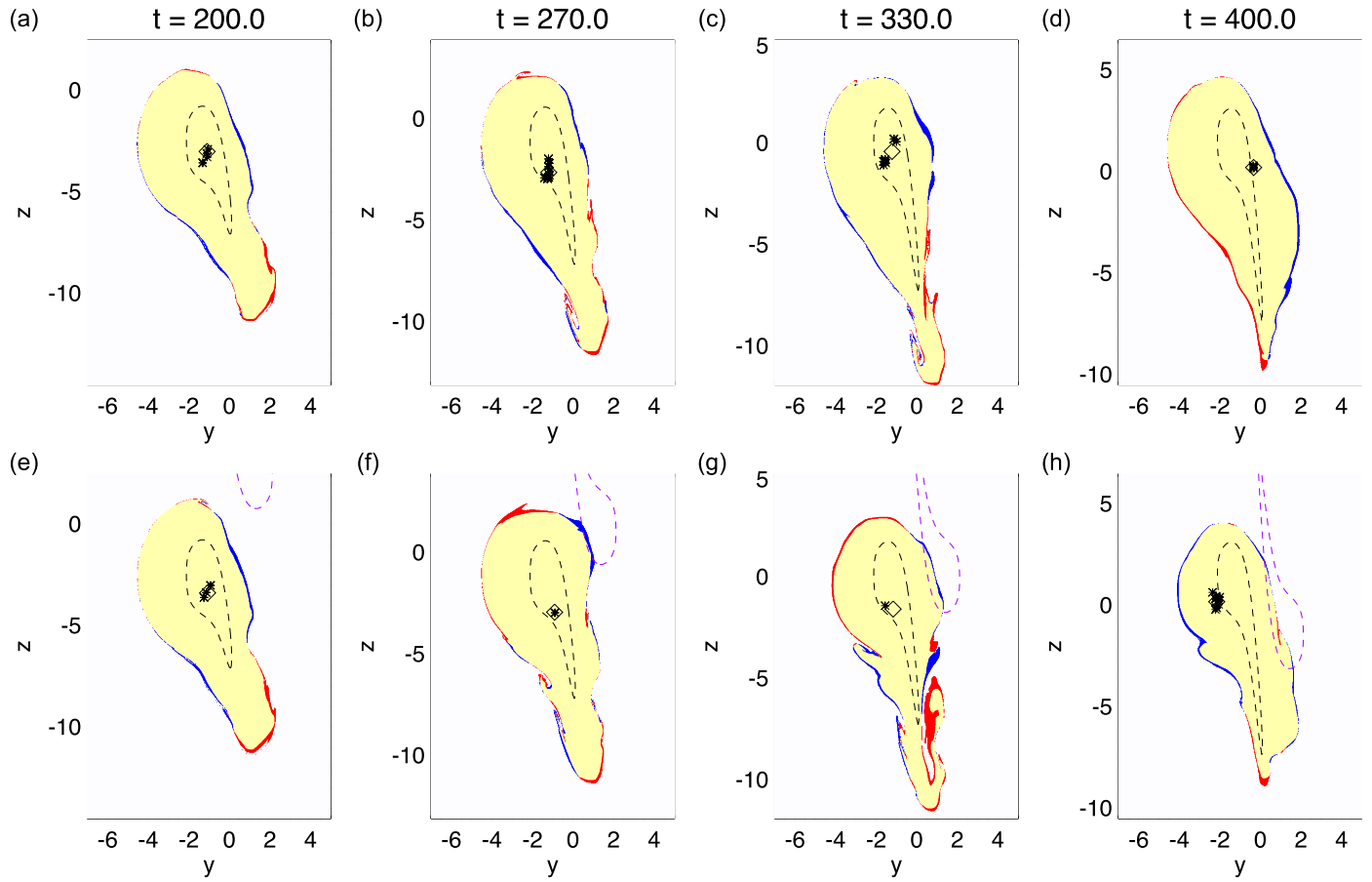

Figure 18. The changing flux domains in configurations 2 (top panels) and 3 (bottom panels) at the same times. Yellow and white show closed and open field regions, respectively. Red and blue show regions of recently opened and closed field, respectively. Asterisks denote the projection of the null point positions. The diamond shows the null centroid (smoothed in time). Dashed black lines show the PIL. The dashed purple line in configuration 3 is a contour of $B_x = -2.0$, outlining the majority-polarity (negative) concentration. An animation is available. The video starts at $t = 10$ and runs to $t = 740$ s. Its duration is 12 s.

(An animation of this figure is available.)

flows induced around the base of the majority polarity, which were absent from the reference simulations used to construct the energies and resulted from field lines diverted around flux bulging laterally at the edge of the majority-polarity concentration. These flows were induced by the surface shear in this region and exhibited no significant jet-like signatures. Once the majority polarity became involved in the jet dynamics, the jet outflows dominated the behavior of ΔK.

Our results demonstrate that the introduction of a second magnetic-flux concentration, with the same polarity as the background, induces additional reconnection and plasma outflows as the two elements approach and recede from each other. However, the basic feature of a localized filament channel repeatedly forming and erupting via the breakout mechanism, as identified in configuration 2, remains the same.

5. Comparison with Observations

We conducted several numerical experiments to understand better the nature of coronal bright points and jets driven by MMEs. Our simulations differ from most previous bright-point models (e.g., Parnell et al. 1994; Priest et al. 1994; Longcope 1998; Galsgaard et al. 2000) in that we consider an open ambient field. We can compare our simulations quantitatively to observations by adopting typical values for length scale, field strength, and plasma density as described in Section 2. Taking $L_s = 2.5 \times 10^8$ cm, $B_s = 2.5$ G, and $\rho_s = 4 \times 10^{-16}$ g cm^{-3} yields $V_s = 1250$ km s^{-1}, $t_s = 2$ s, and $E_s = 9.8 \times 10^{25}$ erg. The width of the separatrix then becomes $\approx 7 \times L_s = 17.5$ Mm, and the null initially sits at a height of $\approx 2.7 \times L_s = 6.75$ Mm. Similar values were found by Zhang et al. (2012) in potential-field extrapolations above two bright points. The background plasma temperature becomes $T \approx 0.94$ MK and the driving speed translates to 25 km s^{-1} and 12.5 km s^{-1} for the fast and slow speeds, respectively. The minority polarity (now with a peak field strength of 62.5 G and magnetic flux of $\approx 8.7 \times 10^{18}$ Mx) is moved a distance of $12 \times L_s = 30$ Mm in each simulation, comparable to the diameter of a supergranule.

In configuration 1S, the field close to the separatrix was sheared, producing steady interchange reconnection modulated by quasi-periodic reconnection bursts. We can roughly estimate the free energy release rate of the steady component from the energy injected before the onset of reconnection in the first 200 time units of the simulation. By $t = 200$, around 2 units of free magnetic energy are injected into the closed field; see Figure 16(a). Accounting for the ramp up of the driver and scaling the values, this corresponds to an energy injection rate of $\approx 5.6 \times 10^{23}$ erg s^{-1} at the maximum driving speed. During the quasi-steady phase, this injection is balanced by losses to numerical diffusion and equates to roughly the free energy available for heating the plasma. Even after accounting for the

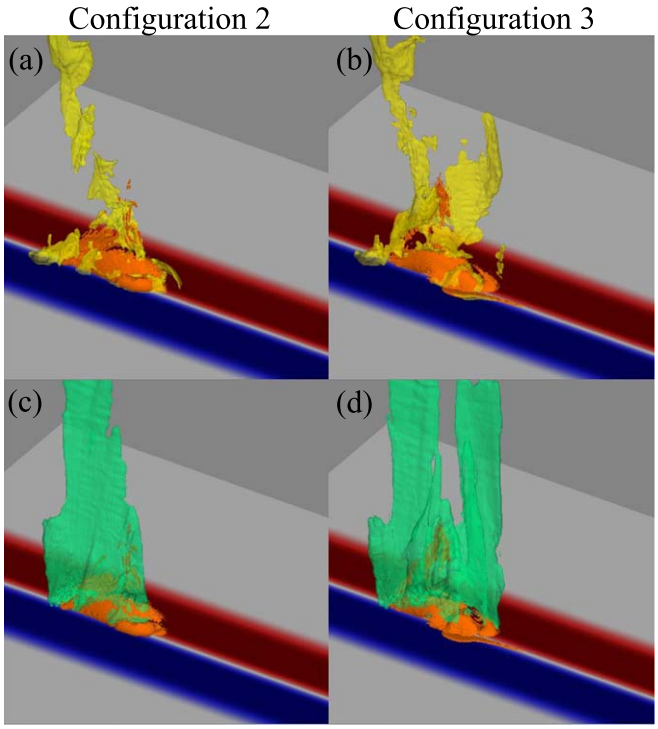

Figure 19. Comparison of the jetting/outflows at $t = 360$ in configurations 2 and 3. Top panels: enhanced mass density ($\rho = 1.1$, yellow isosurfaces). Bottom panels: plasma velocity ($v = 0.05$, green isosurfaces). Orange isosurfaces show current density ($J = 0.3$). Red/blue shading shows the surface plasma velocity v_z; color scale as in Figure 1(b).

unrealistically fast driving speed (see below), this energy release rate compares well with the observed values of 10^{23}–10^{24} erg s^{-1} for bright points (Golub et al. 1974; Priest et al. 1994). The energy released by the bursts was a small fraction of the stored free magnetic energy—$\approx 0.5 \times E_s = 4.9 \times 10^{25}$ erg occurring with a period of $\approx 240 \times t_s = 8$ minutes—while the outflow speeds reached typical values of $\approx 0.05 \times V_s \approx 60$ km s^{-1} along the outer spine. The energy released in each burst corresponds to ≈18% of the energy released over the same period by the steady component. Many bright points exhibit quasi-periodic intensity increases, with periods ranging from a few minutes to a couple of hours (Kariyappa & Varghese 2008; Tian et al. 2008; Zhang et al. 2012). Our results demonstrate that some of this periodicity can be explained by the natural modulation of the interchange reconnection that occurs as minority-polarity elements are moved by surface motions. The predicted outflow speeds, and certainly the periods of the reconnection cycles, are likely too fast because the driving speed (12.5 km s^{-1}) employed in our simulations is too high. However, configuration 1F demonstrated that the cycle period is mainly set by the displacement of the minority polarity. We speculate that, at more typical photospheric speeds (≈1.5 km s^{-1}; e.g., Brandt et al. 1988), the reconnection cycle period would increase by a factor of $12.5/1.5 \times 8$ minutes ≈ 67 minutes, corresponding to the longest observed oscillations in brightness. Without a full treatment of the thermodynamics, however, it is not clear whether the repetitive, low-intensity reconnection jets in this case would be observable.

In configurations 2 and 3, we showed that filament channels periodically formed and erupted as jets when the field near the PIL is strongly sheared. The jets liberated $\approx 3 \times E_s = 2.9 \times 10^{26}$ erg of free magnetic energy, had speeds of $\approx 0.15 \times Vs \approx 190$ km s^{-1}, and durations of ≈90 × t_s = 2.5 minutes. These energies, velocities, and lifetimes are at the lower end of the ranges observed for CH jets (Shibata et al. 1992; Savcheva et al. 2007). Note, however, that our model would predict larger, more energetic jets with different choices for B_s and L_s. Although only two main jets were produced in each simulation, we expect that further shearing and deposition of energy would continue the cycle. The time between the two jets was comparable to (configuration $2 \approx 200 \times t_s$) or faster than (configuration $3 \approx 100 \times t_s$) the time between the reconnection bursts when only the separatrix was strongly sheared. However, this was using the faster (25 km s^{-1}) surface driving speed. Similarly, we then expect that the time between jets would be roughly a factor of 25/1.5 greater, 70–140 minutes, for typical solar surface flow speeds. Periodic jets associated with bright-point flashes with similar periods were described in Zhang et al. (2012).

The periodic bursty dynamics in our simulations follow from the repeated release of energy stored in the closed-field region. Before each burst or jet, the free magnetic energy is built up through an interplay between ideal surface motions shearing the closed field (storing energy) and reconnection opening sheared and closing unsheared field lines (releasing energy). By analyzing simulations at different driving speeds, we found that the timescale for this storage and release is set primarily by the distance the structures are driven, rather than the driving speed itself. This is true provided that the driving motions are slow compared to the coronal Alfvén speed, as occurs on the Sun. Generally speaking, each burst occurs once a threshold of energy storage is reached. The threshold itself is particular to the setup being considered. Once beyond the threshold, some of the energy stored in the closed field is released impulsively over a short time compared with the time for the energy to be stored. The rapid release of energy points to a strong coupling between ideal and non-ideal effects, producing the sharp increase in reconnection rates measured during the bursts and jets. Therefore, ideal and non-ideal effects are present in both the energy buildup phase and the energy release phase. However, it is their coupling in the release phase that leads to the rapid energy releases and bursty dynamics we observe. Such coupling is a general feature of explosive energy release in the corona. It is manifested in these simulations by the upward expansion and ultimate explosive reconnection of the filament channel in the case of jets (configurations 2 and 3), and the similar expansion of the folded field lines and burst of reconnection as they are reconnected in configuration 1. Once a burst or jet occurs, each system returns to slowly rebuilding the stored energy via the interplay of storage via ideal shearing and release via relatively slow reconnection around the null.

In our simulations, the loops of recently reconnected field lines beneath the separatrix are expected to form relatively long-lived bright-point structures. Because our simulations used a simple treatment for the plasma thermodynamics, we cannot directly synthesize observables. However, we obtained a rough estimate of the expected bright-point emission structure in each configuration by using the proxy introduced by Cheung & DeRosa (2012), whereby the square of the current is averaged along field lines before being integrated along the line of sight to create the image. This procedure picks out current-carrying coronal loops and gives a reasonable comparison to observations in EUV, for example. In configuration 1, the relatively unstructured bright point was formed by the recently reconnected loops along one side of the minority polarity (Figure 20(a)). In configuration 2, the main filament

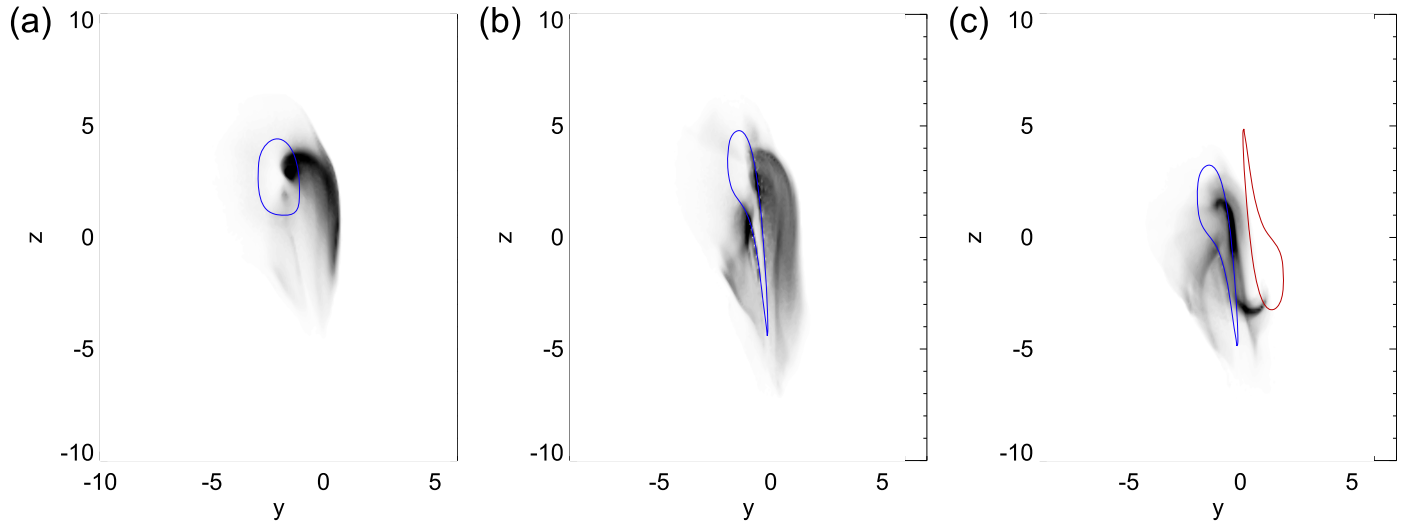

Figure 20. Line-of-sight integrated emission proxy for each configuration. (a) Configuration 1S, $t = 900$. (b) Configuration 2, $t = 500$. (c) Configuration 3, $t = 420$. Reverse gray-scale shading shows the emission proxy, scaled to 75% of the maximum in each. Blue and red contours show $B_x = 2$ and -4, respectively.

channel was localized to the right PIL, producing a bright point with a more complex internal structure than configuration 1 (Figure 20(b)). An additional filament channel appeared to the left of the trailing minority-polarity tail at this time, just before the onset of the second eruption. In configuration 3, a clear sigmoid structure formed between the first and second jets when the filament channel was squeezed between the two passing magnetic elements (Figure 20(c)). The uneven magnetic pressure from the element nearest each end of the filament channel distorted the currents into a sigmoid (e.g., DeVore & Antiochos 2000). Therefore, we have shown that different coronal bright-point morphologies can be realized by altering the way in which the separatrix is sheared and the strength of the flux that passes the minority polarity. The localization of the bright points to one region beneath the separatrix in some events (Galsgaard et al. 2017) may be explained by the results of configuration 1. On the other hand, bright points with more complex structure, and sigmoids (e.g., Brown et al. 2001; Zhang et al. 2012) are more consistent with configurations 2 and 3.

Our modeling also reveals a natural link between bright points and energetic jets. Surprisingly, even when the shear profile was relatively broad, interchange reconnection at the null stripped the shear/helicity from the outer closed field lines to form a localized filament channel adjacent to the PIL. This mechanism is similar to the helicity condensation mechanism (Antiochos 2013), whereby volume-filling reconnections drive magnetic shear/twist toward the boundaries where it collects (PILs) or is removed (separatrices). In our case, the boundary (the separatrix) moves in and out to remove the shear adjacent to it. Consequently, the reach of the mechanism is much more limited, ultimately removing most of the helicity through filament-channel eruption and jet formation. During each eruption, the quasi-steady slow reconnection at the null explosively accelerates for a short time, then resumes a slow rate. Interestingly, the jets have little noticeable rotation, which we attribute to the relatively small flux/energy of the filaments compared with the overall flux/energy of the closed-field region. Together with our previous results (Wyper et al. 2017, 2018), this demonstrates that, depending upon the size and energy of the filament channel, both straight and helical jets can be created by the breakout-jet mechanism and thus can be driven by mini-filament eruptions.

Finally, our results are applicable to other jet- and bright-point-like phenomena involving null points above moving minority-polarity intrusions. At smaller scales, EUV bursts in the chromosphere and transition region exhibit similar features. Recently, Chitta et al. (2017) identified a moving minority-polarity feature in the moat flow from a sunspot that was sheared by surface flows, and attributed the associated EUV brightening to reconnection driven by the shearing. Our results support their conclusions. At yet smaller scales, continually moving and canceling minority magnetic elements are associated with tiny jetlets and plume transient bright points observed at the base of plumes (Raouafi & Stenborg 2014). Raouafi & Stenborg (2014) suggested that the collective action of this energy release helps to power and sustain the plumes. Our results might explain the origin of these plume transient bright points and jetlets. Additionally, the compressive and Alfvén waves launched by the periodic outflows and homologous jets in our simulations may account for the quasi-periodic waves observed within plumes (e.g., DeForest & Gurman 1998; Ofman et al. 1999; Thurgood et al. 2014).

6. Summary

In this work, we studied minority-polarity MMEs in an open background field as a model for coronal bright points and jets. Our main results are as follows:

1. All our simulations exhibited the evolution generic to models with the embedded-bipole topology: free energy build up due to ideal stressing by photospheric motions followed by energy release by reconnection at the null and separatrices. The ideal stressing is always very slow, but the reconnection dynamics vary greatly depending on where the free energy builds up, in particular, how close to the separatrix. For example, if the stressing occurs such that only flux very near the separatrix becomes stressed, then the reconnection becomes essentially steady (e.g., Edmondson et al. 2010). On the other hand, if the stress is concentrated far from the separatrix near the PIL, then the evolution must become

explosive in order to release this free energy (e.g., Wyper et al. 2017).

2. Different bright-point morphologies, from simple loops to sigmoids, can be realized by a combination of the surface shear pattern and the strength and distribution of the flux passing the minority polarity.
3. Steady interchange reconnection driven by the surface motions is modulated by quasi-periodic, low-intensity reconnection bursts that we speculate would correspond to a quasi-periodic brightening of the newly reconnected bright-point loops. Each burst occurs after the minority polarity has been advected roughly its length across the surface.
4. If the surface motions strongly shear the field near the PIL, a filament channel forms. The bright point produces a jet when the filament channel erupts via the breakout mechanism before returning to long-duration, lower intensity bright-point energy release.
5. Additional bursts of reconnection are driven when strong concentrations of the majority polarity pass by the minority polarity, connecting to and then disconnecting from it.

Our results explain several key aspects of observed coronal bright points and jets, and how the two are related. The results aid in further disentangling the complex behavior of such events, which also might contribute to the formation and maintenance of coronal plumes. Many potential extensions of this work should be considered, for instance, the role of the background field inclination angle and the implications of including a more realistic treatment of the atmosphere and coronal energy transport processes. Such extensions are left to future work.

This work was supported through a fellowship award to P.F.W. by the Royal Astronomical Society and grant awards to C.R.D., J.T.K., and S.K.A. by NASA's Living with a Star and Heliophysics Supporting Research programs. Computer resources for the numerical simulations were provided to CRD by NASA's High-End Computing program at the NASA Center for Climate Simulation. Several of the figures were produced using the Vapor visualization package (www.vapor.ucar.edu). We are grateful to P. Kumar, C. E. DeForest, N. E. Raouafi, V. M. Uritsky, and M. A. Roberts for numerous helpful discussions regarding jets and plumes.

ORCID iDs

P. F. Wyper https://orcid.org/0000-0002-6442-7818
C. R. DeVore https://orcid.org/0000-0002-4668-591X
J. T. Karpen https://orcid.org/0000-0002-6975-5642
S. K. Antiochos https://orcid.org/0000-0003-0176-4312
A. R. Yeates https://orcid.org/0000-0002-2728-4053

References

Antiochos, S. K. 1990, MmSAI, 61, 369
Antiochos, S. K. 1996, in ASP Conf. Ser. 95, Solar Drivers of the Interplanetary and Terrestrial Disturbances, ed. K. S. Balasubramaniam, S. L. Keil, & R. N. Smartt (San Francisco, CA: ASP), 1
Antiochos, S. K. 1998, ApJL, 502, L181
Antiochos, S. K. 2013, ApJ, 772, 72
Antiochos, S. K., DeVore, C. R., & Klimchuk, J. A. 1999, ApJ, 510, 485
Brandt, P. N., Scharmer, G. B., Ferguson, S., Shine, R. A., & Tarbell, T. D. 1988, Natur, 335, 238
Brown, D. S., Parnell, C. E., Deluca, E. E., Golub, L., & McMullen, R. A. 2001, SoPh, 201, 305
Cheung, M. C. M., & DeRosa, M. L. 2012, ApJ, 757, 147
Chitta, L. P., Peter, H., Young, P. R., & Huang, Y.-M. 2017, A&A, 605, A49
Craig, I. J. D., & McClymont, A. N. 1991, ApJL, 371, L41
DeForest, C. E., & Gurman, J. B. 1998, ApJL, 501, L217
DeVore, C. R. 1991, JCoPh, 92, 142
DeVore, C. R., & Antiochos, S. K. 2000, ApJ, 539, 954
DeVore, C. R., & Antiochos, S. K. 2008, ApJ, 680, 740
Doschek, G. A., Landi, E., Warren, H. P., & Harra, L. K. 2010, ApJ, 710, 1806
Edmondson, J. K., Antiochos, S. K., DeVore, C. R., & Zurbuchen, T. H. 2010, ApJ, 718, 72
Galsgaard, K., Madjarska, M. S., Moreno-Insertis, F., Huang, Z., & Wiegelmann, T. 2017, A&A, 606, A46
Galsgaard, K., Parnell, C. E., & Blaizot, J. 2000, A&A, 362, 395
Golub, L., Krieger, A. S., Silk, J. K., Timothy, A. F., & Vaiana, G. S. 1974, ApJL, 189, L93
Habbal, S. R., Withbroe, G. L., & Dowdy, J. F., Jr. 1990, ApJ, 352, 333
Haynes, A. L., & Parnell, C. E. 2007, PhPl, 14, 082107
Hong, J., Jiang, Y., Yang, J., et al. 2014, ApJ, 796, 73
Hong, J., Jiang, Y., Yang, J., et al. 2016, ApJ, 830, 60
Innes, D. E., Genetelli, A., Attie, R., & Potts, H. E. 2009, A&A, 495, 319
Kariyappa, R., & Varghese, B. A. 2008, A&A, 485, 289
Karpen, J. T., Antiochos, S. K., & DeVore, C. R. 1996, ApJL, 460, L73
Karpen, J. T., Antiochos, S. K., & DeVore, C. R. 2012, ApJ, 760, 81
Karpen, J. T., DeVore, C. R., Antiochos, S. K., & Pariat, E. 2017, ApJ, 834, 62
Kumar, P., Karpen, J. T., Antiochos, S. K., et al. 2018, ApJ, 854, 155
Lau, Y. T., & Finn, J. M. 1990, ApJ, 350, 672
Longcope, D. W. 1998, ApJ, 507, 433
MacNeice, P., Olson, K. M., Mobarry, C., de Fainchtein, R., & Packer, C. 2000, CoPhC, 126, 330
Masson, S., Aulanier, G., Pariat, E., & Klein, K.-L. 2012, SoPh, 276, 199
Moore, R. L., Cirtain, J. W., Sterling, A. C., & Falconer, D. A. 2010, ApJ, 720, 757
Mou, C., Huang, Z., Xia, L., et al. 2016, ApJ, 818, 9
Nisticò, G., Bothmer, V., Patsourakos, S., & Zimbardo, G. 2009, SoPh, 259, 87
Ofman, L., Nakariakov, V. M., & DeForest, C. E. 1999, ApJ, 514, 441
Pariat, E., Antiochos, S. K., & DeVore, C. R. 2009, ApJ, 691, 61
Pariat, E., Antiochos, S. K., & DeVore, C. R. 2010, ApJ, 714, 1762
Pariat, E., Dalmasse, K., DeVore, C. R., Antiochos, S. K., & Karpen, J. T. 2015, A&A, 573, A130
Pariat, E., Dalmasse, K., DeVore, C. R., Antiochos, S. K., & Karpen, J. T. 2016, A&A, 596, A36
Parnell, C. E., Priest, E. R., & Golub, L. 1994, SoPh, 151, 57
Pontin, D. I., Bhattacharjee, A., & Galsgaard, K. 2007, PhPl, 14, 052106
Pontin, D. I., Hornig, G., & Priest, E. R. 2005, GApFD, 99, 77
Pontin, D. I., Priest, E. R., & Galsgaard, K. 2013, ApJ, 774, 154
Priest, E. R., Parnell, C. E., & Martin, S. F. 1994, ApJ, 427, 459
Pucci, S., Poletto, G., Sterling, A. C., & Romoli, M. 2012, ApJL, 745, L31
Raouafi, N.-E., Georgoulis, M. K., Rust, D. M., & Bernasconi, P. N. 2010, ApJ, 718, 981
Raouafi, N. E., Patsourakos, S., Pariat, E., et al. 2016, SSRv, 201, 1
Raouafi, N.-E., Petrie, G. J. D., Norton, A. A., Henney, C. J., & Solanki, S. K. 2008, ApJL, 682, L137
Raouafi, N.-E., & Stenborg, G. 2014, ApJ, 787, 118
Savcheva, A., Cirtain, J., Deluca, E. E., et al. 2007, PASJ, 59, 771
Shen, Y., Liu, Y., Su, J., & Deng, Y. 2012, ApJ, 745, 164
Shibata, K., Ishido, Y., Acton, L. W., et al. 1992, PASJ, 44, L173
Shibata, K., Nitta, N., Strong, K. T., et al. 1994, ApJL, 431, L51
Shimojo, M., Hashimoto, S., Shibata, K., et al. 1996, PASJ, 48, 123
Sterling, A. C., Moore, R. L., Falconer, D. A., et al. 2016, ApJ, 821, 100
Sterling, A. C., Moore, R. L., Falconer, D. A., & Adams, M. 2015, Natur, 523, 437
Thurgood, J. O., Morton, R. J., & McLaughlin, J. A. 2014, ApJL, 790, L2
Thurgood, J. O., Pontin, D. I., & McLaughlin, J. A. 2017, ApJ, 844, 2
Tian, H., Xia, L.-D., & Li, S. 2008, A&A, 489, 741
Titov, V. S., Forbes, T. G., Priest, E. R., Mikić, Z., & Linker, J. A. 2009, ApJ, 693, 1029
Wang, Y.-M., Sheeley, N. R., Jr., Socker, D. G., et al. 1998, ApJ, 508, 899
Webb, D. F., Martin, S. F., Moses, D., & Harvey, J. W. 1993, SoPh, 144, 15
Wyper, P. F., Antiochos, S. K., & DeVore, C. R. 2017, Natur, 544, 452
Wyper, P. F., & DeVore, C. R. 2016, ApJ, 820, 77
Wyper, P. F., DeVore, C. R., & Antiochos, S. K. 2018, ApJ, 852, 98
Wyper, P. F., DeVore, C. R., Karpen, J. T., & Lynch, B. J. 2016, ApJ, 827, 4
Wyper, P. F., Jain, R., & Pontin, D. I. 2012, A&A, 545, A78
Zhang, J., Kundu, M. R., & White, S. M. 2001, SoPh, 198, 347
Zhang, Q. M., Chen, P. F., Guo, Y., Fang, C., & Ding, M. D. 2012, ApJ, 746, 19